Title
Stress-Strain Response and Fracture Mechanics of the Cuboctahedral Lattice for Aerospace Applications

Author
Gregg, Christine E.

Publication Date
2018

Peer reviewed|Thesis/dissertation

Stress-Strain Response and Fracture Mechanics of the Cuboctahedral Lattice for Aerospace Applications

by

Christine Elizabeth Gregg

A dissertation submitted in partial satisfaction of the

requirements for the degree of

Doctor of Philosophy

in

Engineering - Mechanical Engineering

in the

Graduate Division

of the

University of California, Berkeley

Committee in charge:

Professor Lisa Pruitt, Chair
Professor Oliver O'Reilly
Professor James Evans

Summer 2018

Stress-Strain Response and Fracture Mechanics of the Cuboctahedral Lattice for Aerospace Applications

Abstract

Stress-Strain Response and Fracture Mechanics of the Cuboctahedral Lattice for Aerospace Applications

by

Christine Elizabeth Gregg

Doctor of Philosophy in Engineering - Mechanical Engineering

University of California, Berkeley

Professor Lisa Pruitt, Chair

Architected lattice materials are some of the stiffest and strongest materials at ultra-light density (< 10 mg/cm^3), making them ideal for aerospace structural applications. However, many factors inhibit their use in practical application. The first is scalable manufacturing. Though roll-to-roll process have been developed for 2D lattices, 3D architectured lattice materials rely on manufacturing methods that face scalability challenges when considering aircraft-sized applications. The second challenge is safety. Safety-critical applications demand a high understanding of fracture mechanics and fatigue mechanisms, but the fracture mechanics of lattice materials is a relatively nascent field that has demonstrated several challenges compared to continuum fracture mechanics.

This thesis addresses both of these concerns. The first section presents a discrete lattice material suitable for mass-manufacturing. The mesoscale, ultra-light (5.8 mg/cm^3) fiber-reinforced polymer composite lattice structure is reversibly assembled from building blocks manufactured with a best-practice high-precision, high-repeatability, and high-throughput process: injection molding. The chopped glass fiber-reinforced polymer (polyetherimide) lattice material produced with this method display absolute stiffness (8.41 MPa) and strength (19 kPa) typically associated with metallic hollow strut microlattices at similar mass density. Additional benefits such as strain recovery, discrete damage repair with recovery of original stiffness and strength, and ease of modeling are demonstrated.

The second section characterizes the fracture toughness of the cuboctahedral lattice using experimental and computational methods. Novel experimental methods for use of the compact tension specimen are described, which enable the testing of higher unit cell resolutions than three-point bend fracture bend specimens. 3D printed acrylic compact tension specimens were manufactured and tested with relative densities of 5-15 % and compared to FEA models. The normalized toughness is shown to increase linearly with relative density, matching scaling performance of the higher connectivity octet truss. Effects of specimen geometry are computationally investigated, and limitations of the applicability of long crack fracture theory to cellular materials are discussed. Additionally, a potential toughening mechanism

for lattices is addressed by characterizing crack deflection in a heterogeneous lattice. The He-Hedgepeth criterion for crack deflection in a bi-material is adapted to lattice materials, providing a single parameter to predict crack deflection in a reinforced lattice.

To the late Dr. Benjamin Sim, whose mentoring helped inspire my love of NASA and aeronautics.

Contents

List of Figures

List of Tables

Acknowledgments

My PhD work began and was largely conducted under the guidance of Professor Paul K. Wright. I shall be forever grateful for his mentoring and willingness to let me follow my research passions wherever they lead.

Thank you to Lisa Pruitt for being the best last-minute advisor I could ask for.

I am particularly grateful to have had the chance to work closely with Oliver O'Reilly. Oliver, working on the shoelaces project with you was such a blessing. Your mentoring, thoughtfulness, and character were so appreciated, and I learned much more than dynamics from you. Thank you.

Without the mentoring, guidance, and endless support of my friends and family, none of this would have been possible. This is especially of my parents Elizabeth and Ben, whose support and encouragement are fundamental to all I do. Special thanks to Rose Kantor for being especially supportive through the tough times. My friends: you are too many to name, but your support no less important. Mosaic House, thank you for providing a place to thrive and finish my thesis!

At Berkeley, special shout outs to Pit Pillatsch for being my early academic partner in crime, to Dan Chapman for making everything possible, and the rest of the AME crew for their unwavering support.

A very special thanks to Dr. Kenneth Cheung for allowing my to do research at the Coded Structures Lab, and to Sean Swei for always having sound guidance and an encouraging word.

To Dr. William Warmbrodt, without whom I certainly wouldn't be in a PhD program, and certainly not be working for NASA, and certainly not have found my research passion: your support for students, leadership, and character is an inspiration, a mile-high benchmark that I will strive to meet everyday of my career. Maybe one day I'll come close to a fraction of the positive influence you've had on not only me, but hundreds of students. Thank you.

Chapter 1

Introduction

1.1 Motivation

Aerospace structures are mass critical applications, meaning the total structural mass governs system performance and cost. For space applications, launch remains an expensive endeavor even with commercial space flight reducing in price in recent years. As of 2018, a SpaceX Falcon9 costs $65 million and can carry 22,800 kg to low earth orbit (LEO), 8,300 kg to geosynchronous transfer orbit (GTO), or 4,020 kg to Mars (yet to be demonstrated). The Falcon Heavy is priced at $90 million and can carry up to 63,800kg, 26,700kg, or 16,800 kg to LEO, GTO, and Mars respectively. Reducing structural mass increases the mass that can be allotted to functional payloads, such as sensors, cameras, communication equipment. On Earth, aircraft face similar cost incentives to reduce mass, in addition to environmental motivations for increased efficiency to reduce the carbon footprint of air travel. These cost and performance benefits have motivated interest in light-weight materials with high strength and stiffness.

1.2 Cellular Materials

Many of the lightest materials known are cellular solids, materials that leverage an open microstructure to achieve lower density than their constituent material. Encompassing stochastic foams, lattice materials, many aerogel structures, and natural materials like bone, cork, and honeycomb, cellular materials in general have mechanical behavior that is governed by their microstructural geometry, constituent material, and manufacturing method. Many of the first artificial cellular solids were stochastic foams, cellular solids with a random porous structure (like a sponge) made from polymers or metals. The random microstructure posed a challenge to characterization of the bulk performance of foams until seminal work by Ashby [3] used a representative unit cell to established that the stiffness of a foam can be described by

$$\bar{E} = A\bar{\rho}^a$$

where $\bar{E}$ is relative modulus, the modulus of the lattice normalized by the modulus of the constituent solid, and $\bar{\rho}$ is relative density, the density of the foam normalized by the density of the constituent solid. Later extended to honeycombs, it is now understood that all cellular materials can be described in the same manner. A and a are constant scaling factors dependent on cellular geometry, and A is additionally dependent on material and manufacturing method. A similar scaling relationship was established for relative strength, the strength of the cellular solid normalized by constituent material strength

$$\bar{\sigma} = B\bar{\rho}^{b}$$

This result is only considered valid for brittle elastic materials or the yield strength of elasto-plastic materials. The scaling factors b and B are known to change depending on the relative density regime, as well as lattice geometry, material, and manufacturing method.

Foams have found innumerable applications in everything from lightweight core material for sandwich structures and energy absorption to functional electrodes, but they pay a large performance cost for decreased density. Foams have a stiffness scaling of $a = 2$, meaning that every order of magnitude decrease in relative density corresponds to 2 orders of magnitude decrease in stiffness. Material designers naturally wondered if controlling the microstructure of cellular materials could lead to better performance than random foams at the same densities. Ideally, the stiffness scaling of cellular solids would be $a = 1$, losing only one order of magnitude of stiffness for every order of magnitude loss in relative density. (For stiffness scaling, a cannot be lower than 1, and A cannot be larger than 1.)

This search for ideal scaling lead to the development of architected lattice materials, which use carefully designed microstructures to achieve near ideal scaling. It is now well established in the literature that foams have structures that, for phenomenological reasons, are dominated by beam bending. High performance architected materials choose structures that are dominated by stretching of the beams, leading to stiffer and stronger behavior [8] at the same densities. The resulting ultra-light materials are the stiffest and strongest in the world [41].

Lattice materials are often described in conversation as having high stiffness (or strength) for their weight or density. While this statement is true (they are the stiffest ultra-light materials), it is often conflated with having high specific stiffness. Lattice materials do not have high specific properties. This conclusion can be drawn by examining the scaling equations. Because of the presence of the linear scaling factor (A or B above), the specific strength of lattice materials will always be lower than the constituent solid.

However, lattice materials do very well on other performance metrics. As is well covered in Arnold et al.'s report "Materials Selection for Aerospace Systems" [2], different performance indices characterize the performance of a material for different applications. For example, for a beam in bending, the minimum mass design scales with $\rho/E^{1/3}$. For such a metric, cellular materials offer significantly higher performance that conventional materials at lower densities. These performance benefits motivate the work in this thesis.

1.3 Practical Challenges and Thesis Focus

The ability of architected materials to deliver tuned properties and high stiffness and strength at extremely low densities motivate their use in aerostructures [2, 37]. However, like many new materials, practical challenges currently limit their adoption into critical load-bearing structures. This thesis focuses on addressing two of these challenges in an effort to facilitate faster adoption of these materials in real-world aerospace applications.

One challenge is manufacturing. Like all new materials, moving from lab to application requires the development of scalable manufacturing processes. We discuss current challenges and practices before introducing an emergent solution called discrete lattice materials. This approach uses assembly of a mass manufactured kit of parts to produce high-performance lattices at scale. We show a mass-manufactured, discrete, ultra-light composite lattice material and it's performance in Chapter 2.

The second challenge addressed in this work is the limited understanding of lattice fracture mechanics. From the de Havilland Comet of the 1950s to the 1988 Aloha Airlines Flight 243, aerospace history is sadly replete with examples demonstrating the importance of fracture mechanics and fatigue [40]. To use any material in aerospace, the fracture mechanics of that material must be well understood and sufficient for damage-tolerant design. In part due to manufacturing challenges discussed previously, current understanding of cellular material fracture mechanics is limited in terms of geometries studied and experimental validations performed. In Chapter 3, we review the state of the art in lattice fracture. We then show experimental and computational characterization of the fracture of the cuboctahedral lattice. In Chapter 4, we introduce the idea of heterogeneous lattice materials to enhance fracture toughness. We show that classical frameworks for crack deflection in bi-material can be adapted to lattice materials.

Chapter 2

Ultra-light and Scalable Composite Lattices

2.1 Introduction

The contents of this chapter are published in the journal Advanced Engineering Materials in 2018 under the title "Ultra-light and Scalable Composite Lattice Materials," authored by Christine E. Gregg, Joseph H. Kim, and Kenneth C. Cheung.

Current Manufacturing

Stochastic foams [21] and aerogels [18] can be produced in relatively large quantities, but they feature bend-dominated structures that do not meet the mechanical performance of most architected lattice materials. Conversely, though stretch-dominated architected lattices are some of the lightest and stiffest materials to date, [41] wide-scale implementation has been limited by manufacturing scalability challenges. Printing [7, 23, 42], templating [31, 41], and photolithography methods [24, 41], commonly used to manufacture architected lattice materials, are intrinsically size limited. Though some roll-to-roll manufacturing strategies have been proposed for metallic lattice sandwich structures [29], comparable scalable manufacturing for three-dimensional lattices has yet to be developed.

Building Block Lattice Approach

Manufacturing of cellular materials by assembly of discrete building blocks, each manufactured with conventional best practices, may overcome such limitations. Cheung and Gershenfeld demonstrated assembled ultra-light engineered cellular materials with specific modulus governed by linear scaling [6], and others have showed similar performance at lightweight material mass densities using similar methods [9, 10, 39]. Using this building block approach, we show that near-ideal stiffness and strength behavior can be achieved at ultra-light mass density, using industrial mass production processes. We assemble a lattice

using injection-molded thermoplastic building blocks, produced very quickly (17 seconds per building block) and inexpensively (0.01-0.03 US$ per cubic centimeter). The result is an ultra-light lattice material that, despite theoretical material and geometric disadvantages, displays stiffness and strength behavior in the regime of state of the art metallic and ceramic microlattices. This strategy leverages well-characterized manufacturing processes that can utilize a wide variety of materials. In addition, mass manufacturability, high fidelity behavior prediction with low resolution modeling, and discrete repairability may enable practical wide-scale implementation.

2.2 Methods

Manufacturing and Constituent Material Characterization

Cuboctahedral lattices were assembled from injection molded octahedral unit cells termed voxels (Figure 2.1). Two different constituent materials were tested: Ultem 2200 (20% glass fiber reinforced polyetherimide), and stiffer, more brittle RTP 2187 (40% carbon fiber reinforced polyetherimide). Significant alignment of the chopped fibers within the strut, caused by shear during the injection molding process, was observed in both materials (Figure 2.1(f)). In the case of Ultem 2200, this produced higher effective strength and stiffness than manufacturer data sheet values. Voxels had a pitch, or unit cell length, of 3 inches (76.2mm). Stainless steel size 0-80 bolts and nuts torqued to specification (16 in-oz/ 0.11 Nm) provided reversible and repeatable node connections, which featured a Hirth joint to ensure proper alignment (Figure 2.2(a)) .

Octahedral voxels were produced as monolithic thermoplastic injection molded parts, using custom designed tooling. This tooling was commercially manufactured from hardened steel for operation in a commercial press, with conventional fluid heating according to temperature limits specified for the compounds used (by the compound manufacturers). The complex geometry was achieved using twelve slides, with six larger triangular slides (Figure 2.1(d), blue) forming shutoffs against each other and the two mold halves in groups of four to form struts composing each triangular face of the voxel. Six smaller cylindrical slides (Figure 2.1(d), magenta) formed the fastener holes in each node. Tolerances for the tooling surfaces were specified to less than 25 microns, with the mold cavity (Figure 2.1(e)) scaled according to the coefficient of thermal expansion of the fiber reinforced compound. Complete process cycle time was approximately 17 seconds per part. Voxel struts had a kite shaped strut cross-section detailed in Figure 2.2(b), with a cross-sectional area of 2.63 x 10^{-3} square inches (1.70 mm^2).

To characterize the mechanical behavior of each material, struts were extracted from each voxel type and tensile tested at a strain rate approximating that seen in the assembled lattices (0.0002/s). Figure 2.3 shows characteristic stress-strain curves for both materials. Because of the injection molding process and the geometry of the voxel, knit lines were present in half of the struts (two opposing triangular faces of the octahedron). Knit lines

are where two flow fronts meet in the molding process, creating a local weak point in the part. The mechanical properties of both strut types are reported in Table 2.1 and Table 2.2. Because of the knit line, most knit line struts broke in the gauge length and yielded valid yield strength measurements. This was not true of most struts with no knit line. Therefore, no yield strength (proportionality limit) is reported for those struts.

Voxels were randomly oriented during the assembly process with respect to the location of the knit line struts. For modeling and normalization purposes, the modulus of the lattice assembly was assumed to be dominated by the average modulus of all struts. This is well supported by simulations. Simulations that used only a single voxel orientation (stiffest, worst-cast scenario) were only 2% stiffer than simulations that randomized voxel orientation, which itself differed by less than 5% from simulations using homogeneous struts with the average modulus. For normalization purposes, strength of the lattice assembly was assumed to be dominated by the weakest strut in the lattice.

The relative density of the lattice was calculated by measuring the average mass of each injection molded voxel and the average mass of the nuts and bolts. The average mass of a voxel was 2.01g, with a standard error of 0.0011g or approximately 0.05%. The total mass of the voxels, nuts, and bolts was then divided by the bounding volume of the assembled lattice to yield the density. This was normalized by the density of the constituent polymer, which is the primary load-bearing material in the struts. In an n=4 specimen, where n is the number of voxels per cubic side length, the mass of the bolts was 21% of the total lattice mass and is a penalty that gives the lattice a higher apparent relative density (and thus poorer apparent performance for that given density). In other words, the mass of the bolts is parasitic and does not contribute to stiffness in the lattice.

Table 2.1: Tabulation of measured properties from tensile testing of Ultem 2200 struts, both with (10 specimens) and without (8 specimens) knit lines. Only one strength measurement was valid for the struts without knit lines.

	Modulus (MPa)	Proportionality Limit (MPa)	Ultimate Strength (MPa)
Knit Line Strut Average	5465	93.4	110.6
Knit Line Strut Standard Error	358	5.80	3.08
No Knit Line Strut Average	7032	120.0	144
No Knit Line Strut Standard Error	114	n/a	2.20

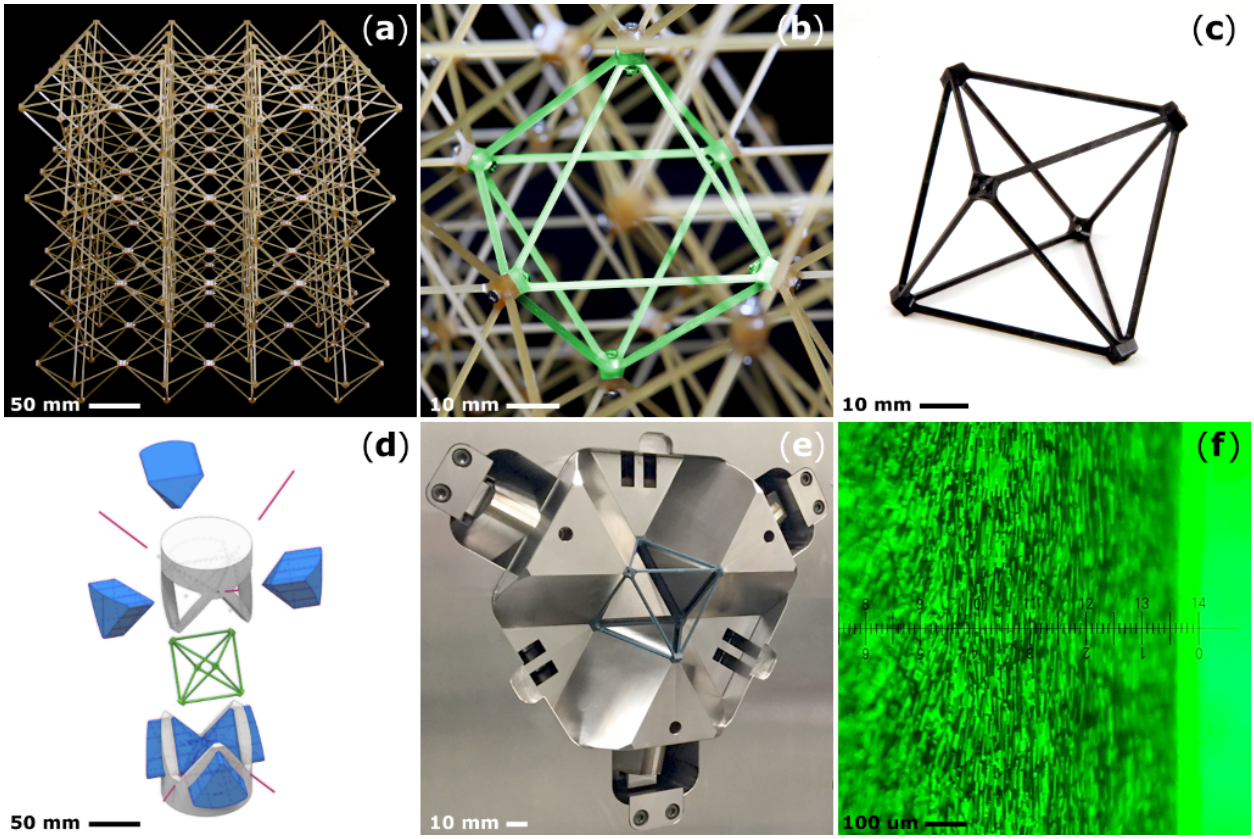

Figure 2.1: (a) An assembled cuboctahedral lattice specimen, made from (b) Ultem 2200 (20% glass fiber reinforced polyetherimide) octahedral unit cells (highlighted), termed voxels. (c) A single monolithic RTP 2187(40% carbon fiber reinforced polyetherimide) injection molded voxel. (d) Exploded view of the injection mold. (e) Picture of the mold surface. (f) Micrograph showing fiber alignment within the RTP 2187 injection molded strut.

Table 2.2: Tabulation of measured properties from tensile testing of RTP 2187 struts, both with (8 specimens) and without (9 specimens) knit lines. Only 5 of the specimens with knit lines had valid proportionality limit strength measurements. None of the specimens without knit lines had valid proportionality limit strength measurements.

	Modulus (MPa)	Proportionality Limit (MPa)	Ultimate Strength (MPa)
Knit Line Strut Average	20993	98.6	110
Knit Line Strut Standard Error	1818	2.47	4.08
No Knit Line Strut Average	33212	n/a	230
No Knit Line Strut Standard Error	893	n/a	9.72

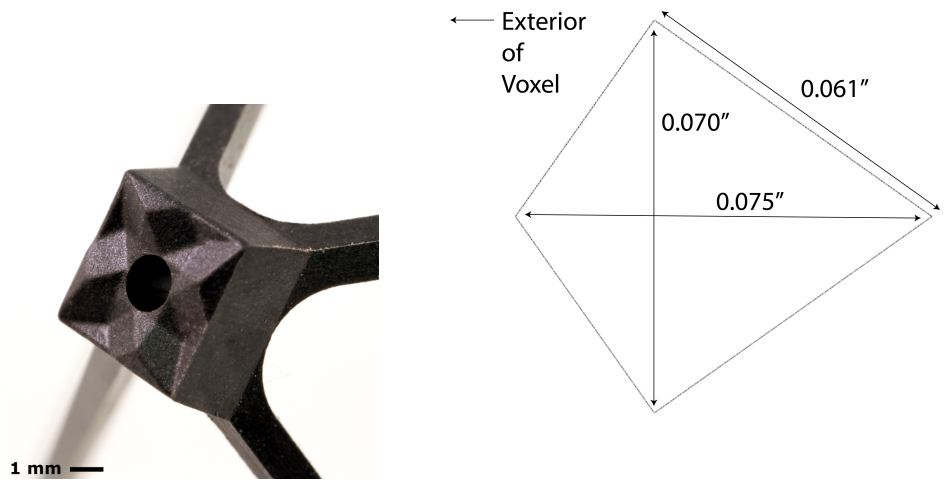

(a) (b)

Figure 2.2: Voxel geometry details. (a) Detail of the node geometry, featuring a hirth joint to ensure proper alignment. The hole accommodates a 0-80 nut and bolt. (b) Cross section geometry of the injection molded struts. The non-rectangular geometry was necessary to enable the slides during the injection molding process.

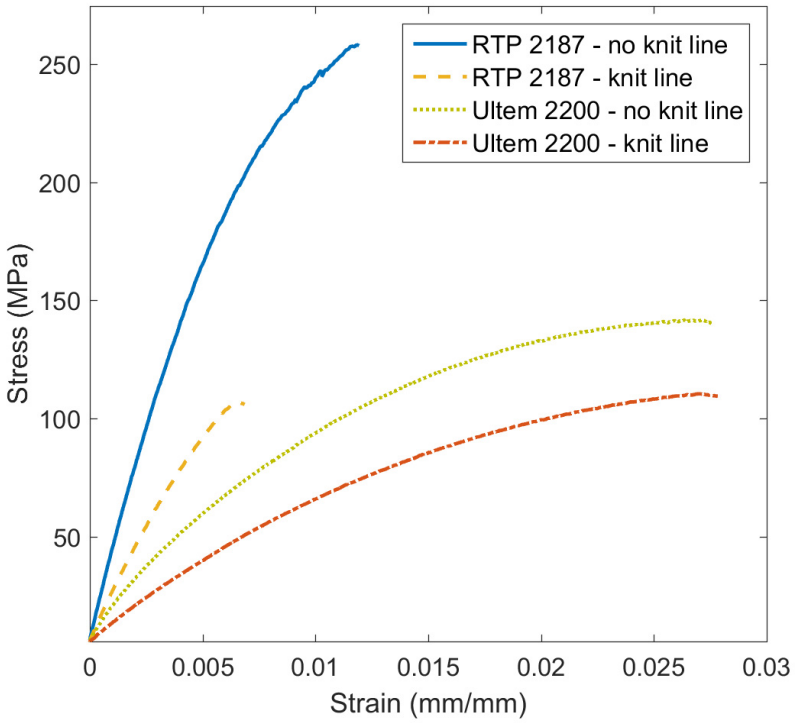

Figure 2.3: Representative curve of a bulk Ultem 2200 and RTP 2187 tension tests, with and without knit lines.

Testing

Various sizes of cubic specimens (n = 1, 2, 3, 4) were assembled from Ultem 2200 injection molded voxels. Each size was tested in triplicate in both tension and compression, first cyclically loaded in the linear-elastic regime, then loaded until failure. The top and bottom surface nodes of each lattice block were bolted to aluminum fixture plates, which were then bolted to an Instron 5982 testing machine. Each specimen size was loaded at a constant strain rate of 0.00066 /s. To characterize a repaired n=2 lattice, the lattice was loaded first in tension using previously described test parameters until a single strut failure. The lattice was then unloaded, the broken voxel was replaced, and the repaired lattice reloaded in tension. The same testing procedure was used for RTP 2187 lattices, but only n=4 specimens were tested in tension and compression.

Simulation

Compression and tension behavior of the Ultem 2200 lattices were simulated using ABAQUS, using the non-linear geometry option to capture large strains. Each voxel contained six nodes and twelve edges, each edge subdivided into four B31 beam elements (three-dimensional Timoshenko beams with linear interpolation). A rectangular element cross section (0.0611in by 0.0429in/ 1.552mm by 1.090mm) was used, selected to equal the second moment of area about the minor kite axis of the actual strut cross section, as well as the total cross sectional area. To increase model fidelity, the finite volume of the node was modeled. The thickness of the node connections was modeled using a single thicker beam matched to the size of the injection molded node (0.15in/3.81mm width, square cross-section, 0.25in/6.35mm long) (Figure 2.4). The average modulus of 6.25 GPa measured from strut testing and a 0.38 Poisson ratio (data sheet value) were used. An ENCASTRE boundary condition (fully constrained) was applied to the bottom nodes, and the top nodes were connected to S4R shell elements (thick shell theory) and constrained to the same z displacement. Forces in the z direction were applied to each node.

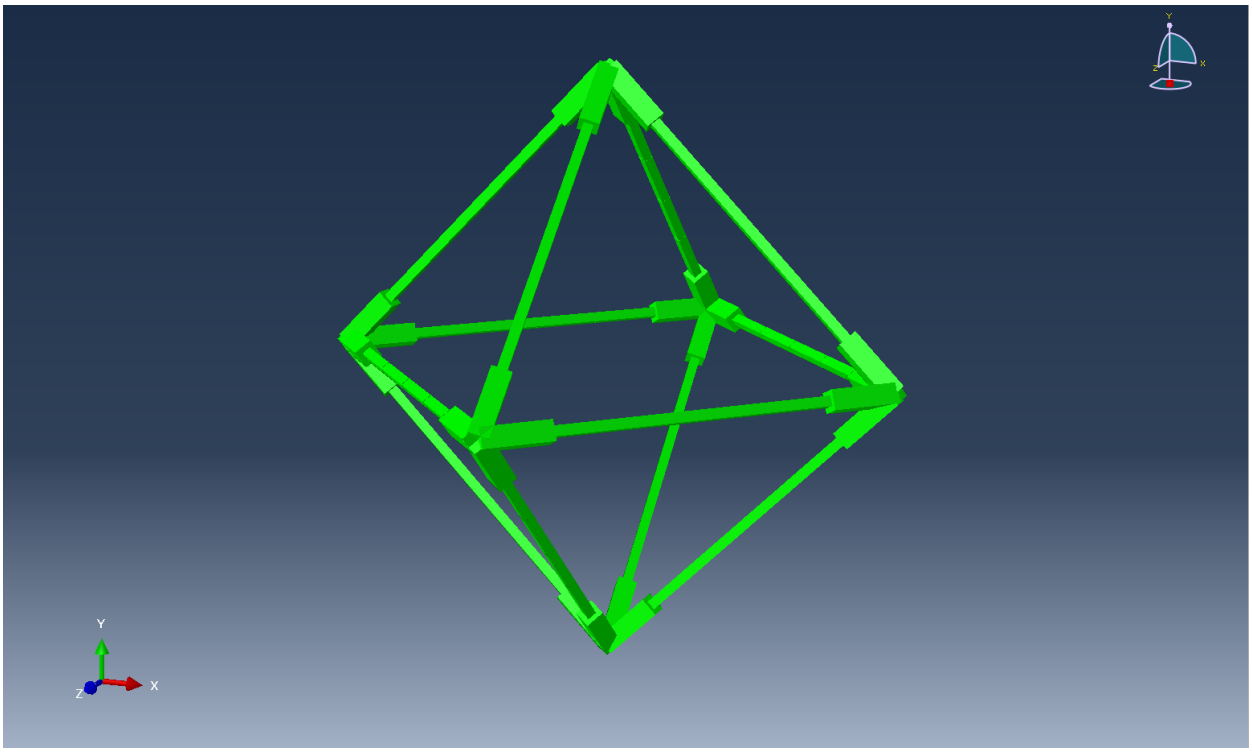

Figure 2.4: Beam profiles of a voxel from the ABAQUS model showing two different beam widths used. The main strut (thinner section) was a rectangular element cross section (0.0611in by 0.0429in/ 1.552mm by 1.090mm), selected to equal the second moment of area about the minor kite axis of the actual strut cross section. The thicker beams modeling the finite size of the nodes had a square cross section 0.15in (3.81mm) wide, and were used to model the effective zero-deflection of the node material .

2.3 Results

Various specimen sizes were tested, each forming a cube with n unit cells per side (total of n^3 voxels per specimen). Converged continuum behavior for modulus was reached by n=4 (Figure 2.5. Symmetric linear elastic behavior in tension and compression was observed for Ultem 2200 lattices, with low hysteresis during cyclic loading (Figure 2.6(a)). Upon initiation of strut buckling, a non-linear elastic region is observed that resembles a bulk yield-like behavior, though with no associated plastic strain (Figure 2.6(b)). Upon unloading, strain and modulus are almost fully recovered (99%). The first reloading into the non-linear region (35% of average break strain) shows a small reduction in the proportionality limit (to 95% of original), which we attribute to small strain setting in the node connections affecting buckling bias. Considerable permanent change in material behavior is only observed after strut breaking initiates.

An ABAQUS FEA model showed outstanding fidelity in the linear-elastic region using a

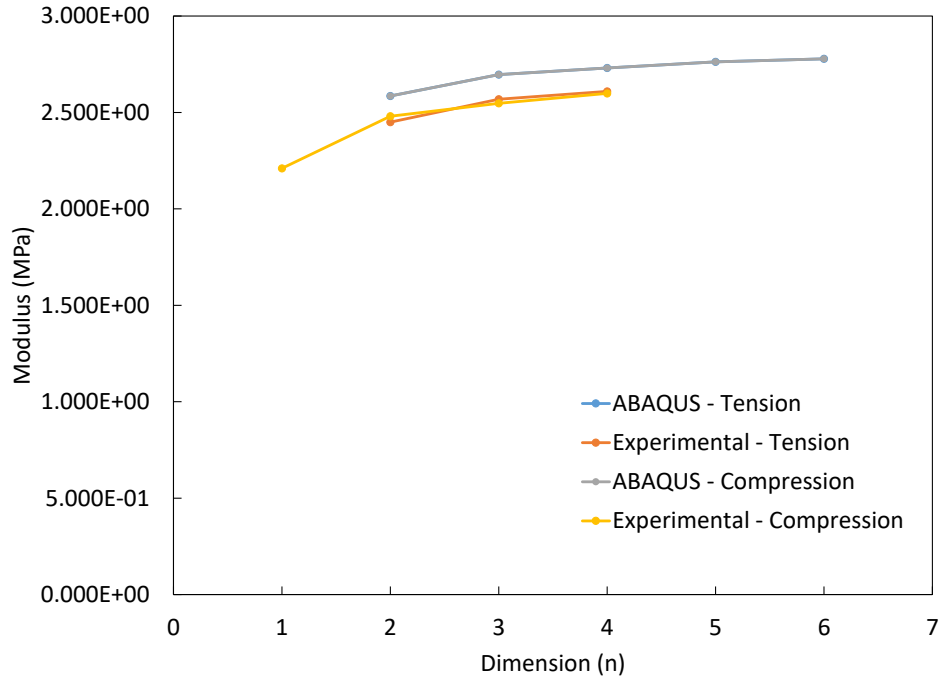

Figure 2.5: Experimental and simulation results showing conversion of sample moduli as sample size (n) increases.

relatively small mesh size, attributed to the discrete nature of the material as a network of beams (Figure 2.7). Modeling results for an n=4 Ultem 2200 lattice predicted a lattice stiffness of 2.71 MPa, which differs by less than 5% from average measured experimental values for tension (2.61 MPa) and compression (2.60 MPa). Discrepancy in predicted yield behavior is attributed to the necessary rectangular approximation of the real kite-shaped strut profile, resulting in small differences in second moment of area and the buckling behavior of the beams.

While linear elastic behavior was symmetric in tension and compression, post-buckling behavior of Ultem 2200 lattices varied in compression and tension (Figure 2.7) and initiated at a lower average stress in compression (10.4 KPa versus 6.28 KPa). When in tension, struts in the plane normal to loading are in compression and eventually buckle (Figure 2.7(b)). After these struts buckle, the material exhibits a bulk hardening effect as deformation modes cause struts originally in tension to further align with the load direction. A similar mechanism is known in stochastic foams [13] and was recently described for two-dimensional architected lattice geometries [36]. After the first few compressed struts break, further bulk hardening

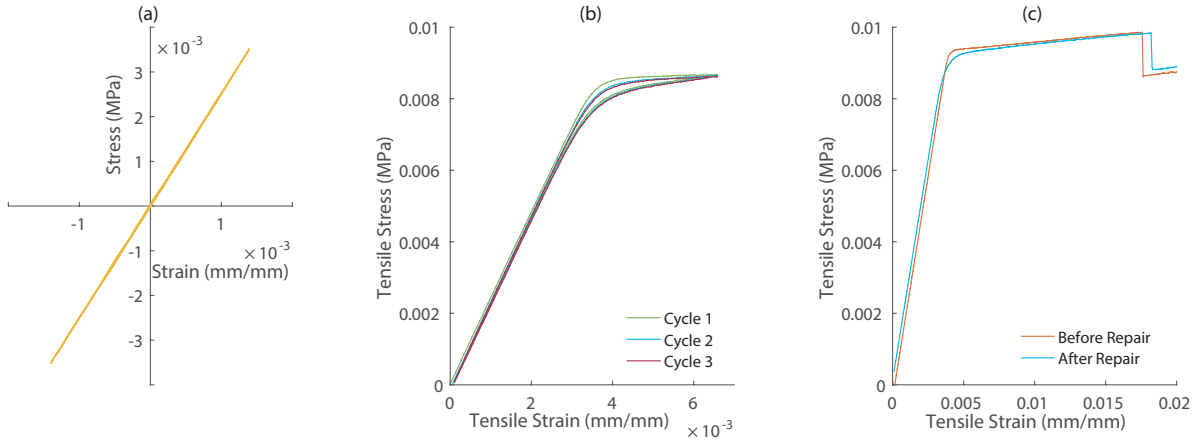

Figure 2.6: (a) Cyclic loading of an n=2 Ultem 2200 lattice in tension and compression in the linear-elastic regime demonstrating symmetric behavior in tension and compression and low hysteresis. (b) Loading (top three curves) and unloading (bottom three curves) of an n=2 Ultem 2200 lattice from the non-linear elastic region shows an initial reset of the proportionality limit (95% of original) attributed to buckling bias and small strain set in the nodes. (c) Stress-strain response of an n=2 Ultem 2200 lattice assembly before and after repair via voxel replacement, each loaded until a single strut failure.

is observed as load alignment continues. Eventually, aligned struts begin to break, and final degradation occurs. The opposite mechanism operated in compression, where struts in the plane normal to loading were in tension (Figure 2.7(d)). Buckling of struts outside of this plane resulted in increased beam-bending dominated behavior and softening after the bulk non-linear transition, before breakage led to continued material failure. Because of the more brittle nature of the RTP 2187 lattices, no post-damage hardening was observed (Figures 2.8).

The assembled lattices demonstrated outstanding behavior upon discrete repair (the replacement of a broken voxel with a new voxel). Figure 2.6(c) shows the stress-strain curve of an n=2 Ultem 2200 sample loaded until a single strut failed. It was then unloaded and the single broken voxel was replaced using the reversible bolted connection. Reloading showed that the repaired structure maintained stiffness equivalent to the original sample (2.52 vs 2.48 MPa), with a small decrease in yield strength (retains 95% of original strength), attributed to strain setting mechanisms discussed previously.

An Ashby chart of relative modulus vs. relative density for ultra-light materials demonstrates the importance of manufacturing process on lattice performance. The relative modulus can be thought of as quantitative measure for how efficiently the manufacturing method and geometry combine to utilize the available performance of a material. Injection molded lattices achieve the same relative stiffness regime as state of the art metallic hollow microlattices (Figure 2.9), despite a 20% mass penalty from nut and bolt hardware and less efficient

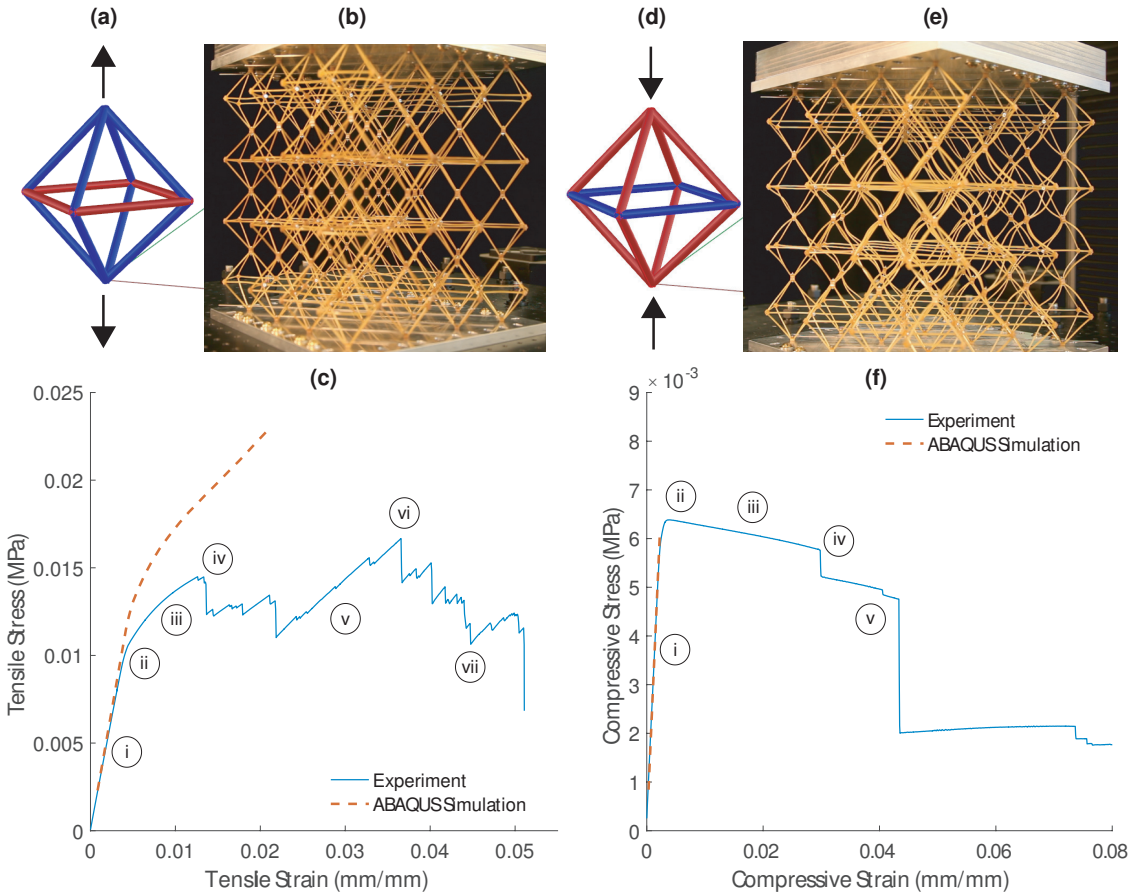

Figure 2.7: (a) Diagram showing which struts are in compression (red) and which struts are in tension (blue) under global tensile loading. (b) Picture showing deformation modes of an n=4 Ultem 2200 lattice under tensile loading. (c) Representative tensile response of an n=4 Ultem2200 lattice assembly and associated simulation results. Distinct behavioral regions of the experimental curve can be seen in (i) linear elastic behavior, (ii) initiation of strut buckling and non-linear elastic regime, (iii) hardening caused by alignment of struts with load direction due to buckling deformation, (iv) first strut failure, (v) second hardening regime caused by continued strut alignment with load, (vi) ultimate strength, and (vii) final degradation with continued strut failure. (d) Diagram showing which struts are in compression (red) and which struts are in tension (blue) under global compressive loading. (e) Picture showing deformation modes of an n=4 Ultem 2200 lattice under compressive loading. (f) Representative compressive response of an n=4 Ultem2200 lattice assembly and simulation results. Distinct behavioral regions of the experimental curve can be seen in (i) linear elastic response, (ii) initiation of strut buckling and non-linear elastic behavior, (iii) softening as buckling causes strut misalignment with load, (iv) first strut failure, and (v) catastrophic strut failure and continued degradation.

solid struts [26]. Both types of injection molded cuboct lattice outperform an assembled uni-directional CFRP cuboct lattice of higher relative density.[6] Since they use the same geometry, this difference can be attributed to manufacturing. The same behavior is observed in absolute modulus (Figure 2.9(b)), where injection molded lattices are competitive with metallic and ceramic microlattices.

Injection molded lattices achieve the same regime of relative strength as other architected lattice materials (Figure 2.10). The difference between the RTP 2187 and Ultem 2200 relative strength is attributed to their differing degrees of ductility and strut buckling strength (per modulus). The strength of cellular materials is known to be controlled by different mechanisms based on the relative density. At high relative density, strength is governed by the stretching strength of struts. But at lower relative density, the strength is governed by the buckling strength of struts, which is dependent on the modulus of the constituent material. For this reason, the transition to buckling controlled relative strength (and the associated quadratic scaling) happens at lower relative densities for lower modulus materials. We see this in the injection molded cuboct lattices. Though the strut geometry is the same, the buckling load for the Ultem 2200 struts is much lower than for RTP 2187 because of the approximately 3x lower stiffness. Therefore, Ultem 2200 lattice yields at a lower strength in compression which, along with Ultem 2200s higher ductility, results in much more lattice ductility before the first broken strut. In contrast, the RTP 2187 lattice shows limited evidence of yield and ductility before break in compression, which suggests that the stiffer and more brittle struts do not buckle before breaking.

Table 2.3: Average performance values and associated standard error for n x n x n Ultem 2200 lattices tested in tension. The proportionality limit is the transition from linear to non-linear elastic behavior. The break strength is the stress at which the first strut breaks. The ultimate strength is the highest stress sustained by the material. Tension data for a single voxel was not taken.

	Modulus (MPa)		Proportionality Limit (MPa)		Break Strength (MPa)		Ultimate Strength (MPa)	
n	Avg.	SE	Avg.	SE	Avg.	SE	Avg.	SE
1	n/a	n/a	n/a	n/a	n/a	n/a	n/a	n/a
2	2.45E+00	5.14E-02	9.37E-03	3.10E-05	9.85E-03	4.60E-05	1.06E-02	8.10E-04
3	2.57E+00	2.48E-02	1.06E-02	1.95E-04	1.35E-02	3.88E-04	1.46E-02	3.58E-04
4	2.61E+00	1.21E-02	1.04E-02	9.81E-05	1.46E-02	1.66E-04	1.74E-02	3.89E-04

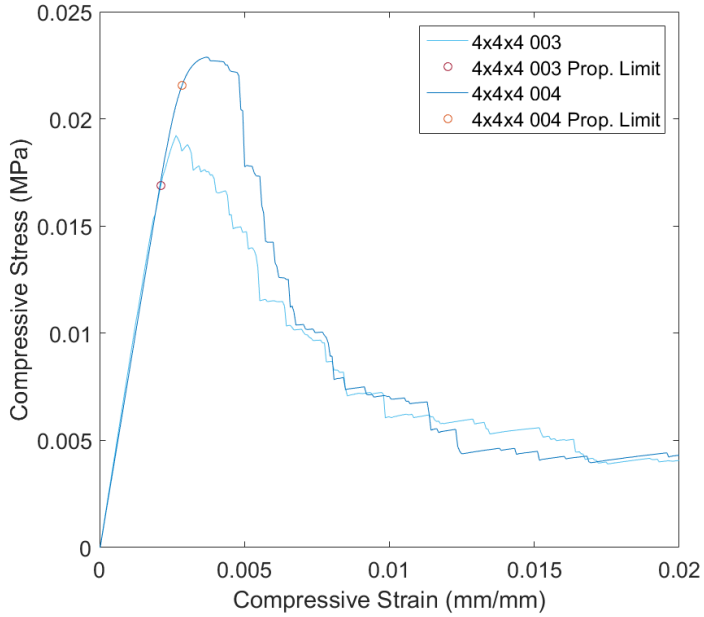

(a)

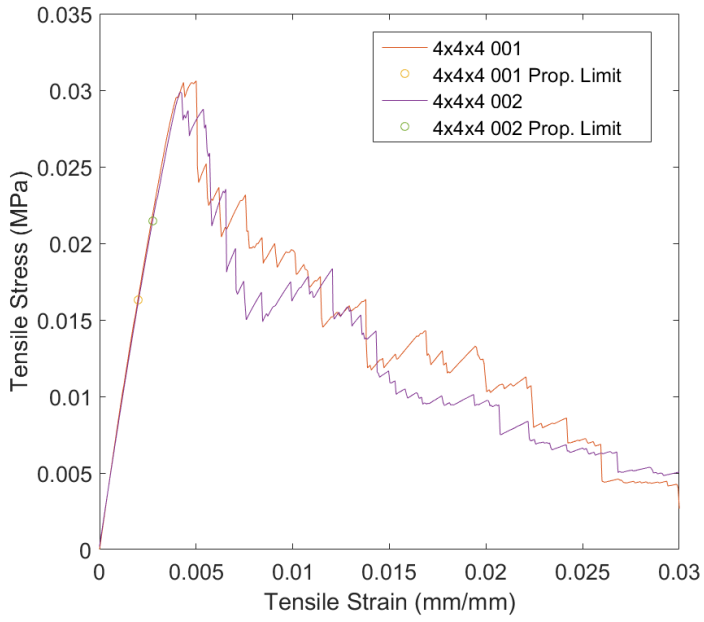

(b)

Figure 2.8: (a) Stress strain curves of all $n = 4$ RTP 2187 specimens tested in compression and associated proportionality limits. (b) Stress strain curves of all $n = 4$ RTP 2187 specimens tested in tension and associated proportionality limits.

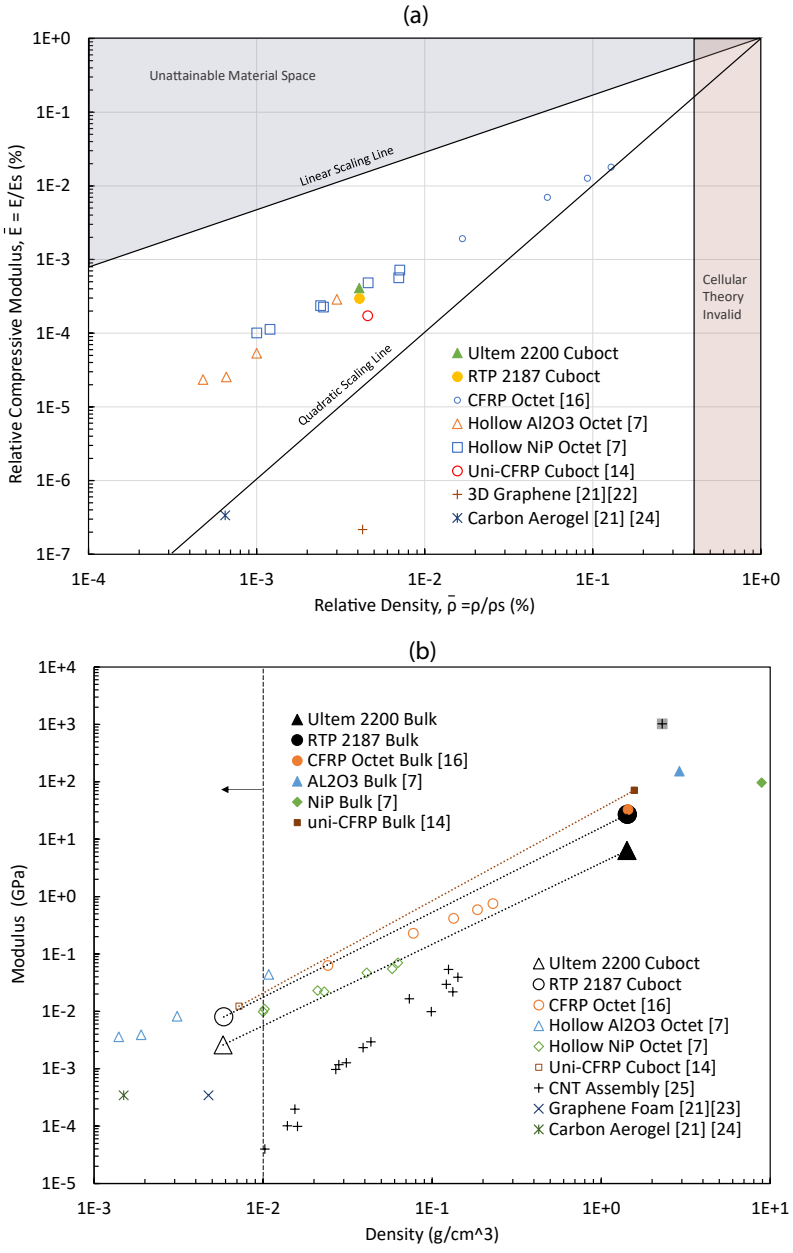

Figure 2.9: (a) A comparison of ultra-light materials shows the high relative performance of injection molded lattices (n=4) (b) Injection molded lattices achieve the same absolute performance regime as ceramic and metallic hollow microlattices. Dotted lines compare the scaling of injection molded cuboct lattice with an assembled unidirectional CFRP cuboct lattice, [6] demonstrating how higher relative performance of RTP 2187 cuboct causes the convergence of performance. Values from this work were normalized with the average measured strut stiffness of the respective material.

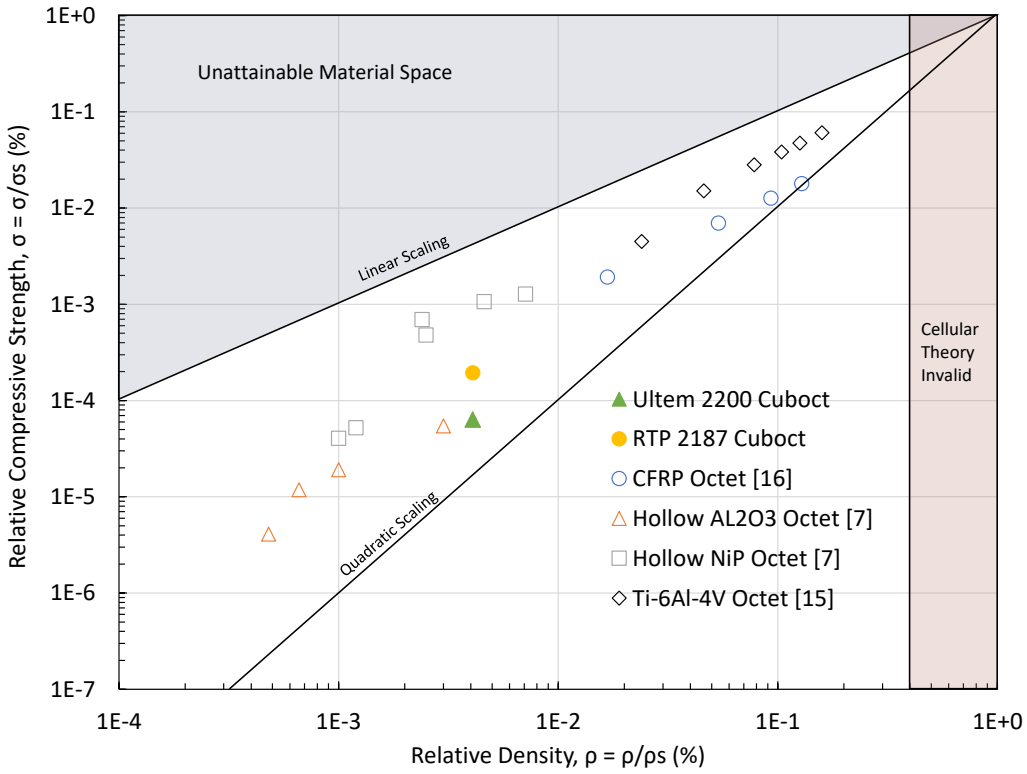

Figure 2.10: Injection Molded lattices achieve the same regime of behavior as other ultra-light lattices. Values from this work were normalized with yield strength of the weakest strut in a voxel.

Table 2.4: Average performance values and associated standard error for n x n x n Ultem 2200 lattices tested in compression. The proportionality limit is the transition from linear to non-linear elastic behavior. The break strength is the stress at which the first strut breaks. The ultimate strength, defined for tension as the highest stress sustained by the material post break, is not meaningful for compression specimens because they were not tested to densification. Therefore, the highest stress sustained was the proportionality limit.

	Modulus (MPa)		Proportionality Limit (MPa)		Break Strength (MPa)		Ultimate Strength (MPa)	
n	Avg.	SE	Avg.	SE	Avg.	SE	Avg.	SE
1	2.21E+00	1.71E-02	6.80E-03	1.41E-04	6.97E-03	1.22E-04	n/a	n/a
2	2.48E+00	2.98E-03	6.91E-03	2.12E-05	6.01E-03	7.81E-05	n/a	n/a
3	2.55E+00	2.40E-02	6.61E-03	8.52E-05	6.03E-03	4.72E-05	n/a	n/a
4	2.60E+00	2.46E-02	6.28E-03	7.83E-05	5.78E-03	3.38E-05	n/a	n/a

Table 2.5: Tabulated results for testing of $n = 4$ RTP 2187 cuboct. Results for each specimen are listed, as well as average properties for the modulus, proportionality limit, and break stress, the stress at which the first strut broke. For RTP 2187 cuboct, the break stress was also the ultimate strength for both tension and compression.

Specimen #	**Modulus (MPa)**	**Proportionality Limit (MPa)**	**Break Strength (MPa)**
1 (tension)	8.59E+00	1.63E-02	3.05E-02
2 (tension)	8.24E+00	2.14E-02	2.99E-02
3 (compression)	7.99E+00	-1.69E-02	-1.92E-02
4 (compression)	7.95E+00	-2.15E-02	-2.29E-02
Tensile Average	**8.41E+00**	**1.89E-02**	**3.02E-02**
Standard Error	**1.22E-01**	**1.81E-03**	**2.16E-04**
Comp Average	**7.97E+00**	**-1.92E-02**	**-2.11E-02**
Standard Error	**1.57E-02**	**1.64E-03**	**1.29E-03**

2.4 Conclusions

By demonstrating injection molded lattices, we show that selecting materials for manufacturability with traditional, high-precision processes can create lattices with state of the art performance while offering many additional benefits. Assembly from building blocks that took seconds to make and an unconstrained build envelope offer true mass manufacturability, in addition to discrete repairability. Especially with combination with recent advances in manufacturing robotics, this strategy may enable production of complex assemblies at mass production scale that achieve high-performance ultra-light material properties. The specific mechanical performance advantages are particularly relevant to applications with critical dynamic modes, such as aerospace structures, with performance metrics that scale with the square or cube root of stiffness per mass density [2]. Building block based assembly provides opportunities spanning the material lifecycle, potentially streamlining design, analysis, manufacturing, and servicing to fully realize the potential of lattice materials in transformative structural applications.

Chapter 3

Fracture of the Cuboctahedral Lattice

3.1 Introduction

In the quest for ever stiffer and stronger lightweight materials, architected lattice materials have demonstrated the ability to access ultralight densities while maintaining outstanding material properties [6, 31]. Like traditional cellular solids such as foams, bone, and wood, architected lattice materials take advantage of an open microstructure to achieve low density. However, unlike traditional cellular solids with microstructures governed by transverse beam bending, architected lattice materials use carefully engineered microstructural geometry to create stretch governed behavior with higher performance [8]. This microstructural control yields extremely tunable materials with high stiffness and strength at light and ultra-light densities [9, 10, 41], appealing for applications in aerospace [2, 38]. A large body of both computational and experimental work exists to describe and predict the strength and stiffness of such materials [8, 13, 31, 41], but less is known about their fracture properties. Understanding fracture in architected cellular materials is vital to implementation in safety-critical load-bearing applications.

Like many other material properties for cellular solids, the fracture toughness of a given lattice geometry is easily understood as a function of its relative density. Pioneering work by Ashby and Gibson [3] showed that the normalized mode 1 fracture toughness of a cellular solid (traditional or architected lattice), K_{norm}, scales with the relative density such that

$$K_{norm} = \frac{K_{IC}}{\sigma_f \sqrt{\pi l}} = D\left(\frac{\rho}{\rho_s}\right)^d = D\rho_{rel}^d \tag{3.1}$$

where K_{IC} is the lattice mode 1 plane-strain fracture toughness, l is the lattice strut length, σ_f is the failure strength of the strut material, ρ is the lattice density, ρ_{rel} is relative density, and ρ_s is the density of the constituent material, and D and d are constants. The exponent d is geometry dependent, with lower values being favorable, and describes how the fracture toughness of a lattice of a given geometry will decreases at density decreases, relative to the strength of the starting material. It is interesting to note that fracture toughness of a

lattice is not dependent on the fracture toughness of the constituent material, but rather on the strength (though consideration of manufacturing flaws would bring fracture toughness considerations into the determination of σ_f). Ashby's derivation for traditional stochastic foams predicts $d = 3/2$, which shows good agreement with experimental results [3].

The fracture behaviors of many two-dimensional lattice geometries have been investigated, largely through finite element computational methods. Most well studied is the honeycomb geometry, one of the few whose analytical and computational results have been validated experimentally [12, 16, 20, 27]. Fleck and Qiu compared honeycomb to other two dimensional geometries [11] and demonstrated the strong geometry dependence of lattice fracture behavior beyond the typical bend vs. stretch dominated topology classification sufficient for modulus scaling prediction [8]. Crack-tip fields for various two dimensional geometries have also been calculated [35].

Understanding of fracture in three dimensional lattice geometries is less mature. The fracture of the Kelvin lattice (tiled tetrakaidecahedrons) was simulated and shown to match the relative density scaling seen in stochastic foams [22]. Three-point bend studies have shown linear fracture toughness scaling of the octet lattice [25] and 3/2 scaling of a diamond cell lattice [28], though the latter maybe be better understood as a quasi two-dimensional geometry.

Motivated by the geometry dependence suggested by Fleck and Qiu, this study seeks to characterize the fracture behavior of an alternative three-dimensional geometry, the cuboctahedral lattice, hereafter referred to as cuboct. A design for a compact tension fracture specimen adapted for cellular materials is presented and manufactured with 3D printing to validate computational predictions.

Geometry

The cuboct geometry consists of node-connected octahedral unit cells (Figure 3.1), termed voxels. Interest in the cuboct geometry is motivated by its demonstrated linear stiffness scaling at lower connectivity than other linearly scaling lattices (octet) [6]. The idealized relative density, $\bar{\rho}$, which calculates the volume of struts of node to node length and accounts for node volume by way of the spatial overlap of the struts, is given by

$$\bar{\rho} = 3\sqrt{(}2)\left(\frac{t}{l}\right)^2 \tag{3.2}$$

where t is the strut thickness and l is the strut length. However, the manufacturing of any lattice must include a finite node volume. To account for this, an exact relative density including node volume for the non-ideal printed geometry (Appendix A) was calculated, and is reported in Table 3.1. As expected, the disparity between the ideal relative density predicted by 3.2 and the exact calculation is largest (10%) at the highest relative density calculated (0.15). Full discussion on the exact relative density calculation and comparison with the idealized case can be found in Appendix A.

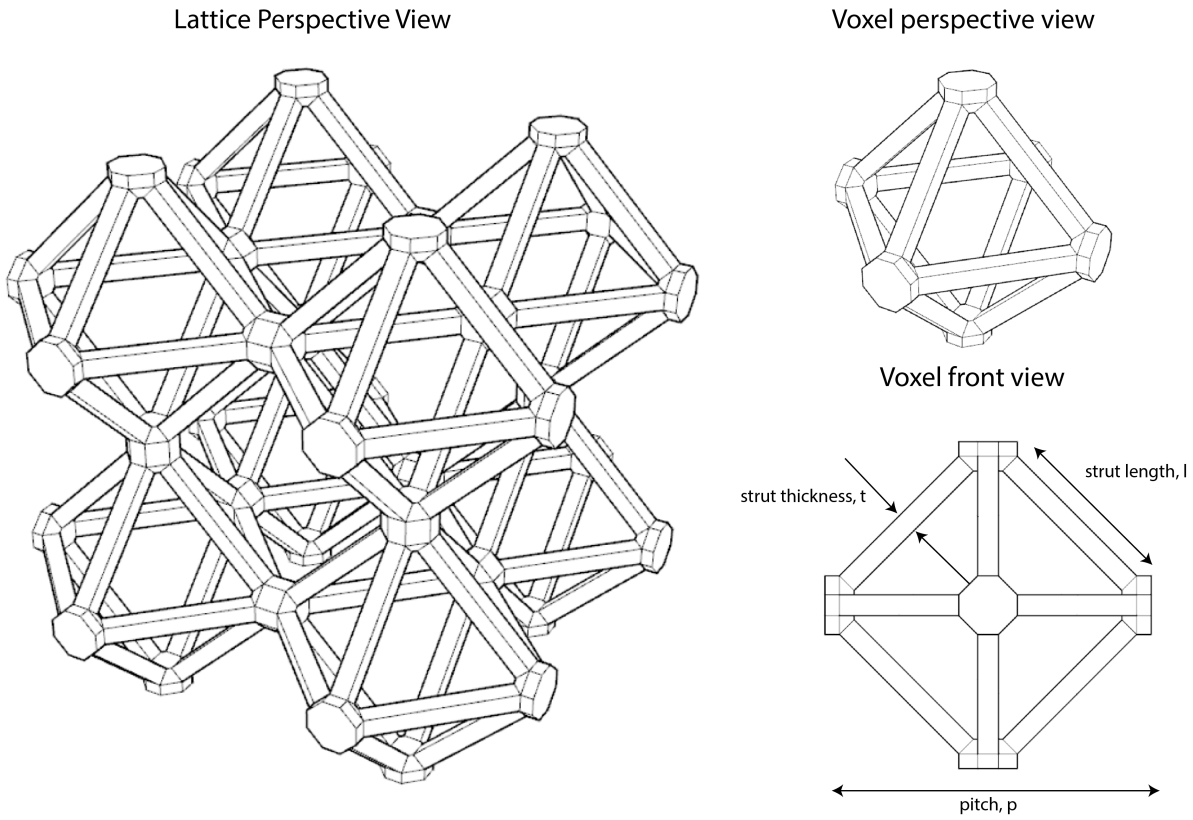

Figure 3.1: Cuboctahedral geometry, consisting of vertex connected octahdra unit cells termed voxels.

3.2 Methods

To facilitate comparison with standard solid materials, this work seeks to apply standard fracture mechanics theory to characterize the fracture of the cuboctahedral lattice. As is *de rigeur* when using traditional standards with new materials, we consider the assumptions within those standards and their application to this type of material. The continuum assumption implicit in the development of fracture mechanics theory raises fundamental questions about its applicability to cellular materials, which easily exist at unit cell scales coarse enough to poorly approximate a continuum material. The validity of continuum treatment of the lattice affects the applicability of many dimensions, such as the stress intensity factors for given specimen geometries.

Early FEA work established that an a/p, the crack length normalized by lattice unit cell length, equal to 7 for brittle honeycombs [20] and 10 for brittle foams [19] was required for the applicability of long-crack continuum mechanics theory, and proposed a correction factor to account for the reduced fracture toughness associated with shorter cracks. Additionally, the aspect ratios of honeycombs were found to affect the necessary a/p for long-crack theory.

This suggests that the number of unit cells per characteristic length necessary for continuum behavior is geometry dependent, and motivates the numerical investigation of resolution and specimen size effects. Thus, fundamental to the experimental investigation of cuboct fracture is the computational investigation of the effect of lattice resolution and specimen size.

This work proceeds in two parts. The first assumes relative convergence of continuum properties for the cuboct lattice at $a/p = 10$ to design and test compact tension fracture specimens. These experimental results are compared to numerical investigations in part 2, investigating the expected validity of the experimental results and suggesting improved geometric corrections.

Experimental Specimen Design and Fabrication

The compact tension geometry was chosen to address concerns about continuum behavior. Compact tension specimens for lattices maximize the resolution of characteristic specimen lengths for a given specimen size. For example, at a desired resolution of a/p=10 (suggested by prior literature to be a conservative value), the largest dimension on a 3-point bend specimen with dimensions recommended by ASTM would be 80 unit cells, whereas the largest dimension on a compact tension specimen is only 26. This lends itself to additive manufacturing methods, for larger specimens can be printed in a constrained build volume. The design of the compact tension specimen (Figure 3.2) was adapted from ASTM E399 [4]. Specimens were manufactured using an inkjet type 3d printer (3d Systems Projet 3600; 37 micron layer thickness) and thermoset acrylic material (VisiJet M3-X; Material Properties available in 3.1). Extensive testing was conducted to characterize printed bulk material performance and validate consistency in the printed process, described in the following section. Given the nature of the print material, results are expected to characterize the fracture behavior of brittle materials. Solid interfaces were printed into the lattice to contact the loading pins and crack mouth opening displacement sensor (Figure 3.2). Four different relative densities were tested (5%, 7%, 10% and 15%), each with a 500 micron strut width and varying lattice pitch (Table 3.1. Relative densities were chosen to span the largest possible density range given print bed size limitations. Each specimen was printed with an initial crack length, a, of 10 unit cells, suggested to be above the unit cell crack length necessary for long crack theory validity [19, 20].

Specimen Pitch (mm)	**Relative Density**	**Strut Thickness (mm)**
3.85	0.159	0.500
4.81	0.100	0.500
5.77	0.068	0.500
6.81	0.049	0.500

Table 3.1: Pitch (unit cell size) and strut length for various relative density specimens

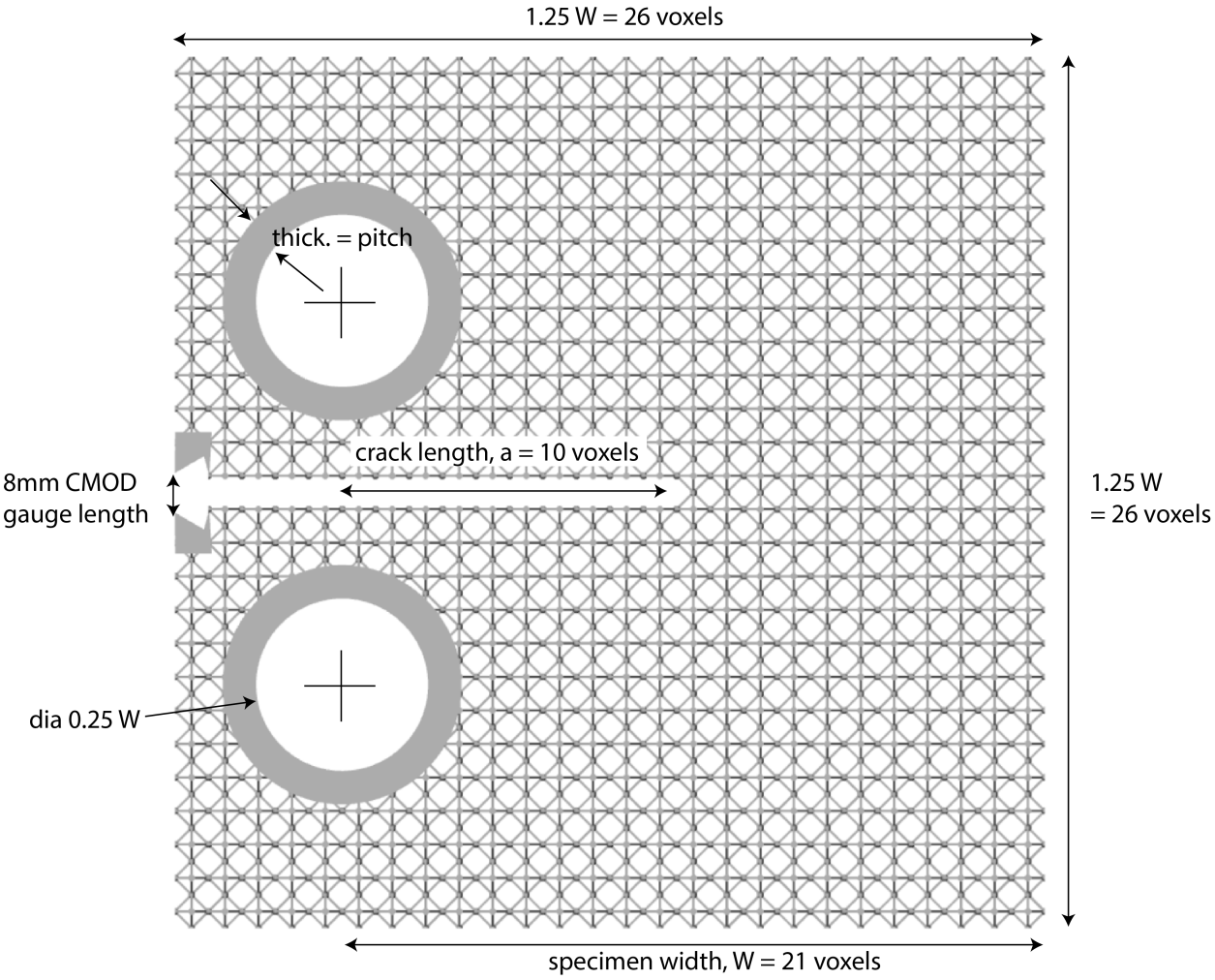

Figure 3.2: Compact tension specimen

Material Processing and Characterization

A Projet 3600 polyjet printer on ultra-high resolution mode (37 micron layer thickness) was used to print specimens with Visijet M3-X material (manufacturer reported properties in Table 3.2). Five dogbone tensile specimens compliant with ASTM D638 were printed in each of the x, y, and z print directions and tested at 5mm/min extension rate (check with ASTM D638). The results are presented in Table 3.3, and representative stress-strain records are shown in Figure 3.3 . As is expected for this type of printing, x and y print directions (in-plane) show comparable properties, whereas the z print direction demonstrates less stiffess, strength, and ductility. This is expected due to the poorer cohesion between print layers than within layers. While anisotropy is acknowledged, because all specimens are printed in the same orientation, and because the z print directions aligns through the thickness of the c(t) specimens, anisotropic effects are results are expected to be minimal.

Material Property	Condition	Datasheet Value
Density @ 80C (liquid)	ASTM D4164	1.04 g/cm^3
Tensile Strength	ASTM D638	49 MPa
Tensile Modulus	ASTM D638	2168 MPa
Elongation at Break	ASTM D638	8.3 %
Flexural Strength	ASTM D790	65 MPa

Table 3.2: Reported data sheet properties for Visijet M3-X

	Modulus (MPa)	Yield Strength (MPa)	Yield Strain (mm/mm)	Ultimate Strength (MPa)	Ultimate Strain (mm/mm)
X Average	1893 ± 11	35.1 ± 0.4	0.0190± 6.9E-5	45.6± 0.5	0.0528± 3.7E-3
Y Average	1842 ± 3	34.7± 0.4	0.0193± 2.1E-4	45.6± 0.1	0.0702± 1.6E-3
Z Average	1713 ± 7	29.9± 0.4	0.0176± 3.5E-5	30.6± 0.8	0.0184± 8.7E-4

Table 3.3: Average tensile properties and standard errors for dogbone tensile specimens printed in each principle print direction, tested according to ASTM D638.

All lattice specimens were printed with support material (VisiJet S300), which was melted away from the model in a 65C convection oven. Care was taken to use absorbent pads to wick away as much residue support wax as possible. As can be seen in Figure 3.4, some residue wax remained. However, the effect of this can be neglected due to the order of magnitude difference in stiffness of the model material and the wax and the relative size of the wax layer and the strut size. Additionally, since the wax layer was consistent from specimen to specimen, it can be expected to not influence the studied scaling behavior.

The properties of bulk printed lattice were tested. Compression specimens consisted of 10 voxel edge length cubes printed with 2mm thick loading plates. While we acknowledged that these plates constrain boundary conditions and do not yield a true compressive modulus, issues associated with even loading of the specimen necessitated plates that ensured more reliable results. Additionally, modeling results suggested that the boundary effect was minimal. Support wax was melted from each specimen using a 65C oven, as was done for fracture specimens. For each relative density used in the fracture specimens, a triplicate compression sample was tested using a strain rate of 0.00167 /s, first cyclically and then to failure (Figure 3.5). Figure 3.5 shows a loading region before 5 mm/mm strain due to slight warping in the printed plates. Linear regression on failure curves had r^2 in excess of 0.988, and we therefore treat the printed lattice materials as approximately linear elastic, with a yield strength equal to the failure strength of the material. Compliance corrections were applied to the modulus data to account for the printed plates, and both the corrected and uncorrected modulus measurements (calculated using a linear regression fitted to linear portion of the data) are presented in Figure 3.6. Strength results are presented in Figure

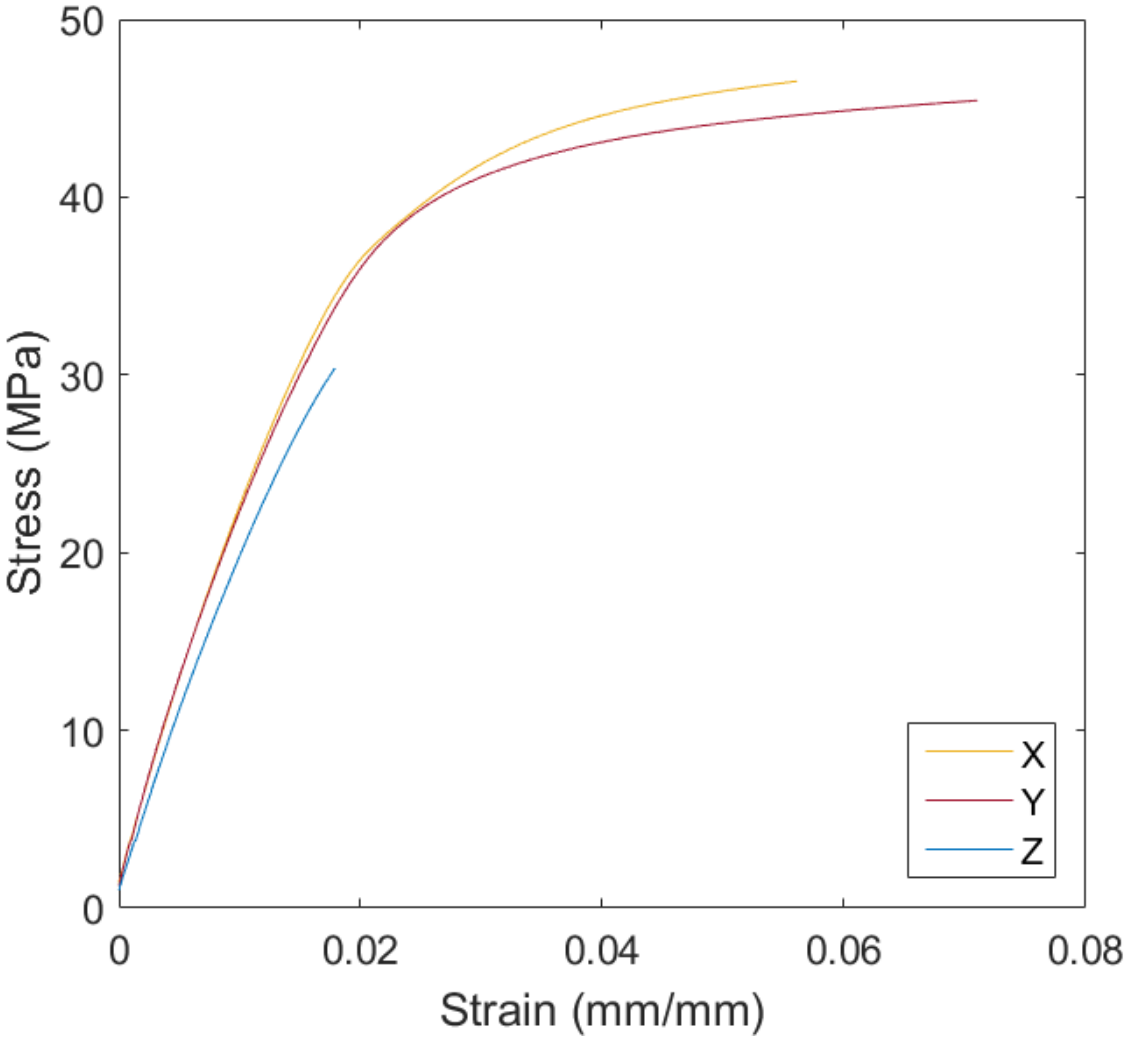

Figure 3.3: Representative tensile stress-strain records for printed dogbone tension specimens for each of the three print directions. As is generally expected for this print type, x and y print directions (in-plane) shown comparable properties, whereas the z print direction demonstrates less stiffness, strength, and ductility. This is expected due to the poorer cohesion between print layers than within layers.

3.7.

To ensure the quality of printed lattices, testing was conducted to determine the strut width that provided consistent properties. Using the same method and specimen design described previously for bulk compressive modulus and strength measurements, various lattices with equivalent relative density (0.1) but different strut lengths were evaluated, each loaded at a strain rate of 0.00017/s. Figure 3.8 shows these strength results, which show a settling

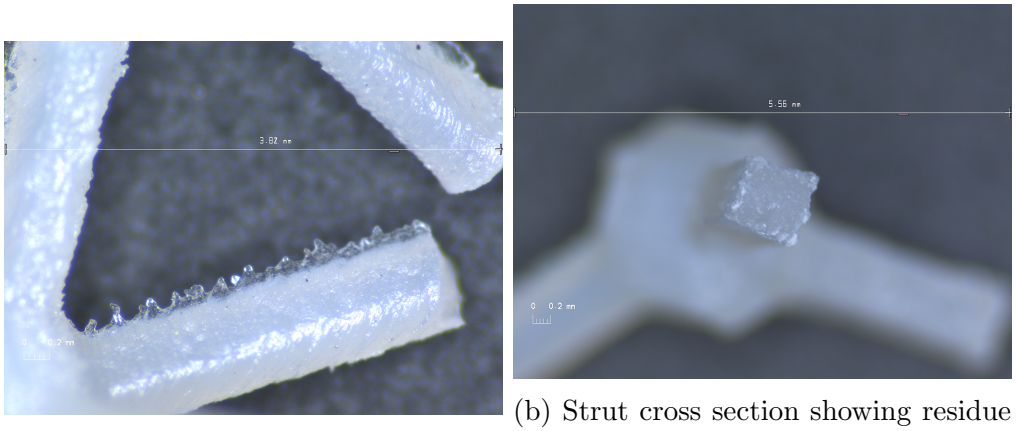

(a) Wax residue showing melt flow

(b) Strut cross section showing residue thickness

Figure 3.4: Wax residue on processed lattices

of the average value of 0.500 mm strut width. This 0.500 mm strut width was taken as a minimum strut size to provide stable material properties. Modulus results showed similar convergence.

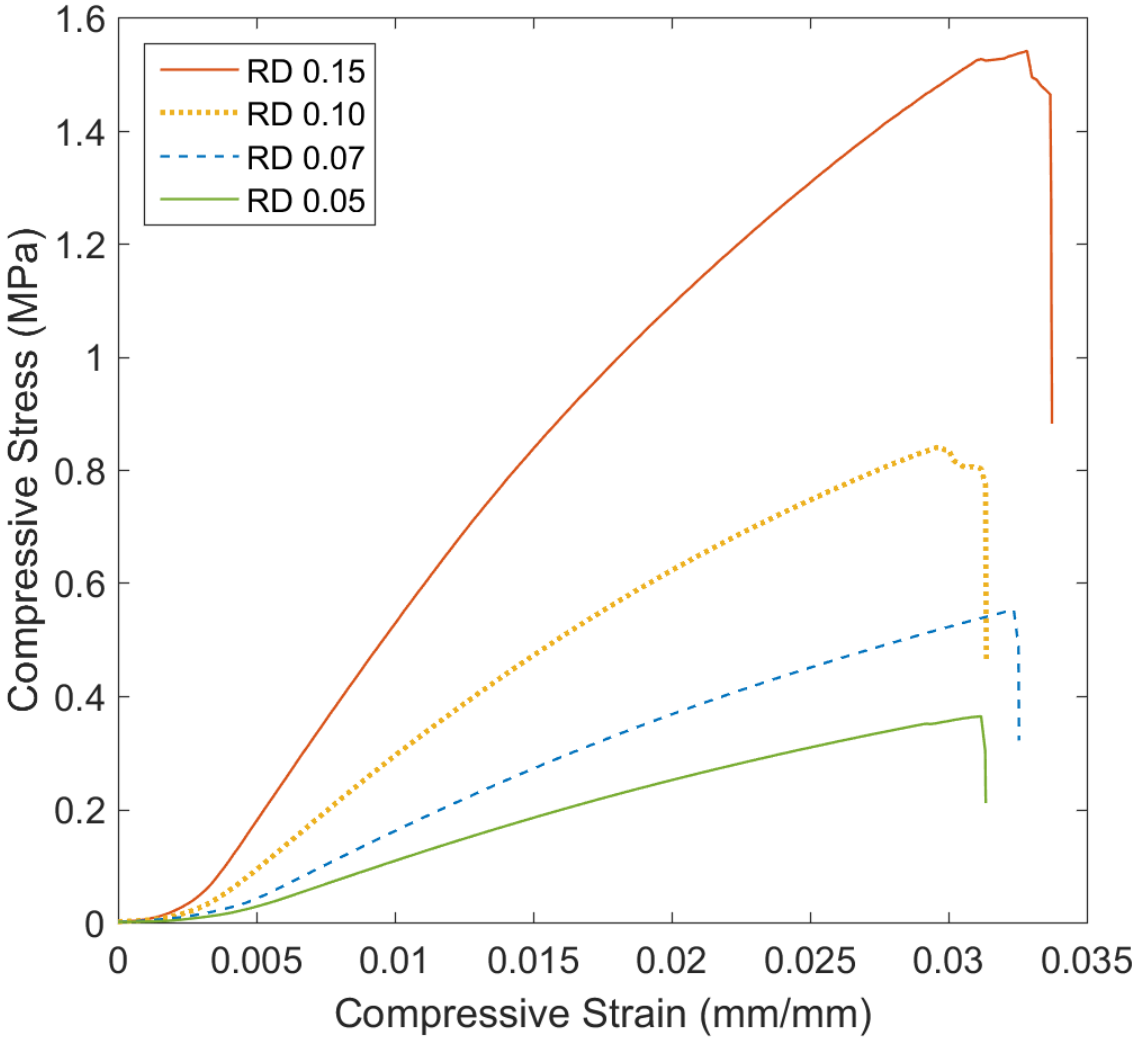

Figure 3.5: Representative curves from compression testing of 10 voxel edge length cubes of each relative density specimen testing in fracture. Initial hardening during loading is due to progressive contact of the loading platen with the printed plates, and are not indicative of hardening behavior in the lattice.

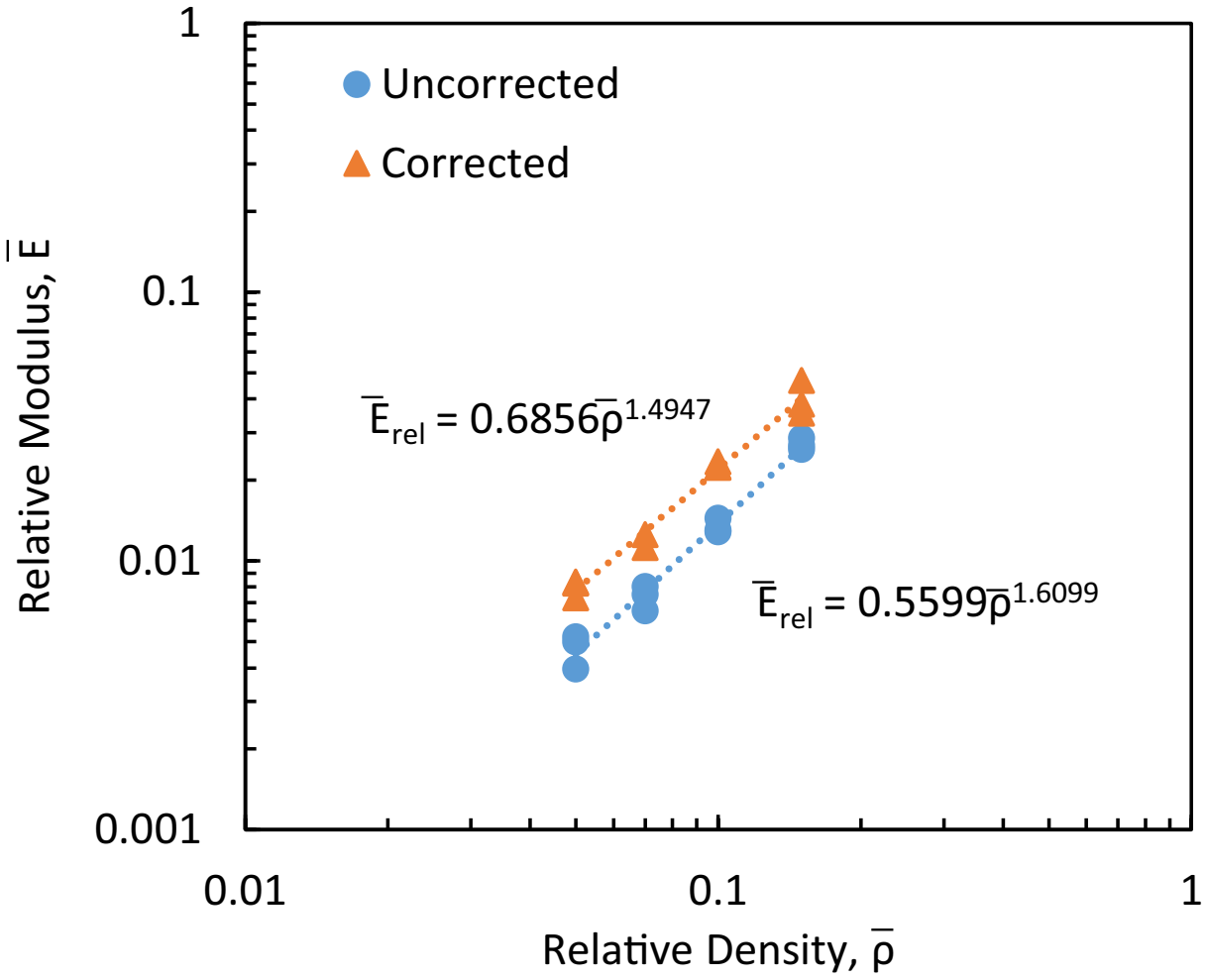

Figure 3.6: Scaling of compressive modulus with relative density for printed cuboct specimens, both raw uncorrected data and compliance corrected data.

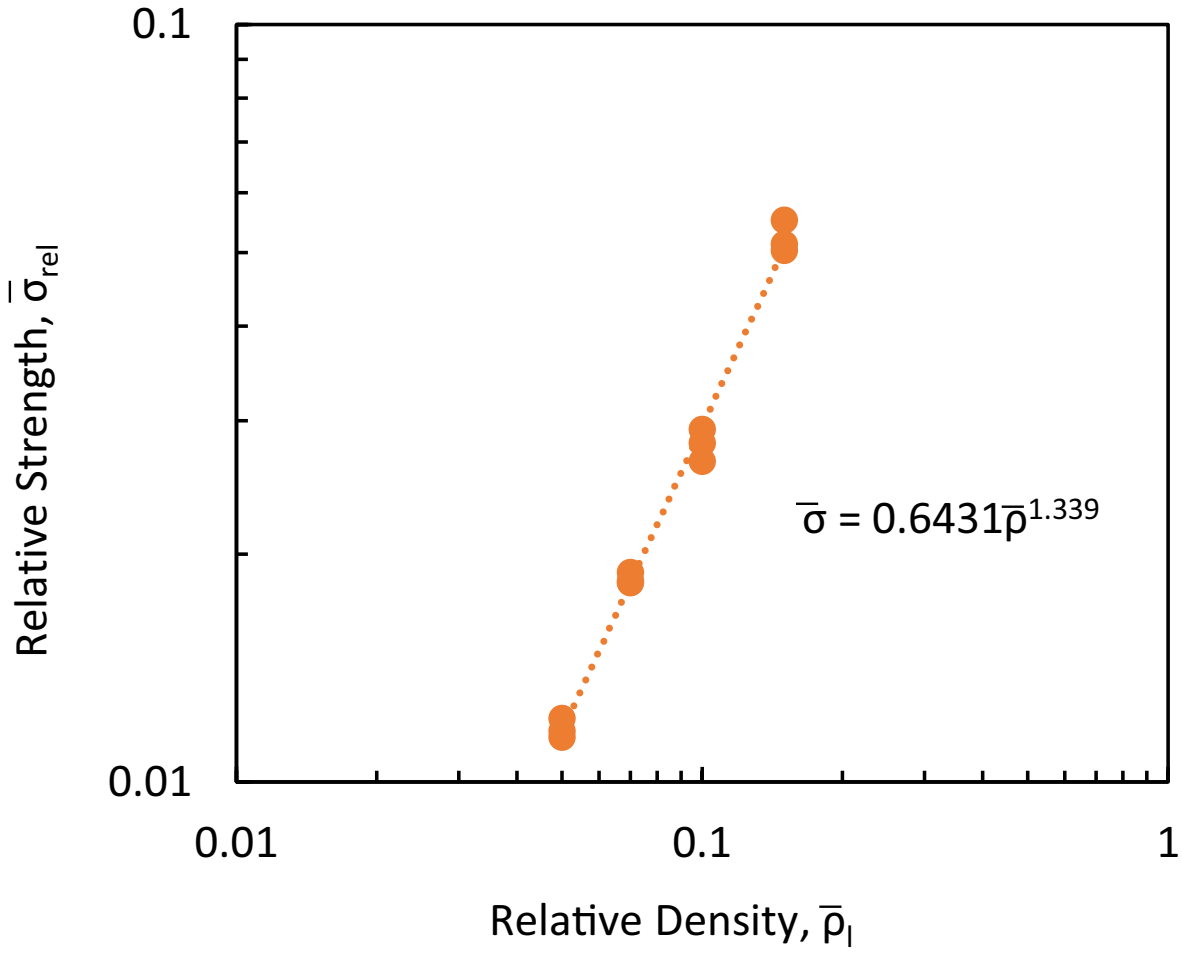

Figure 3.7: Scaling of compressive ultimate strength with relative density for printed cuboct specimens.

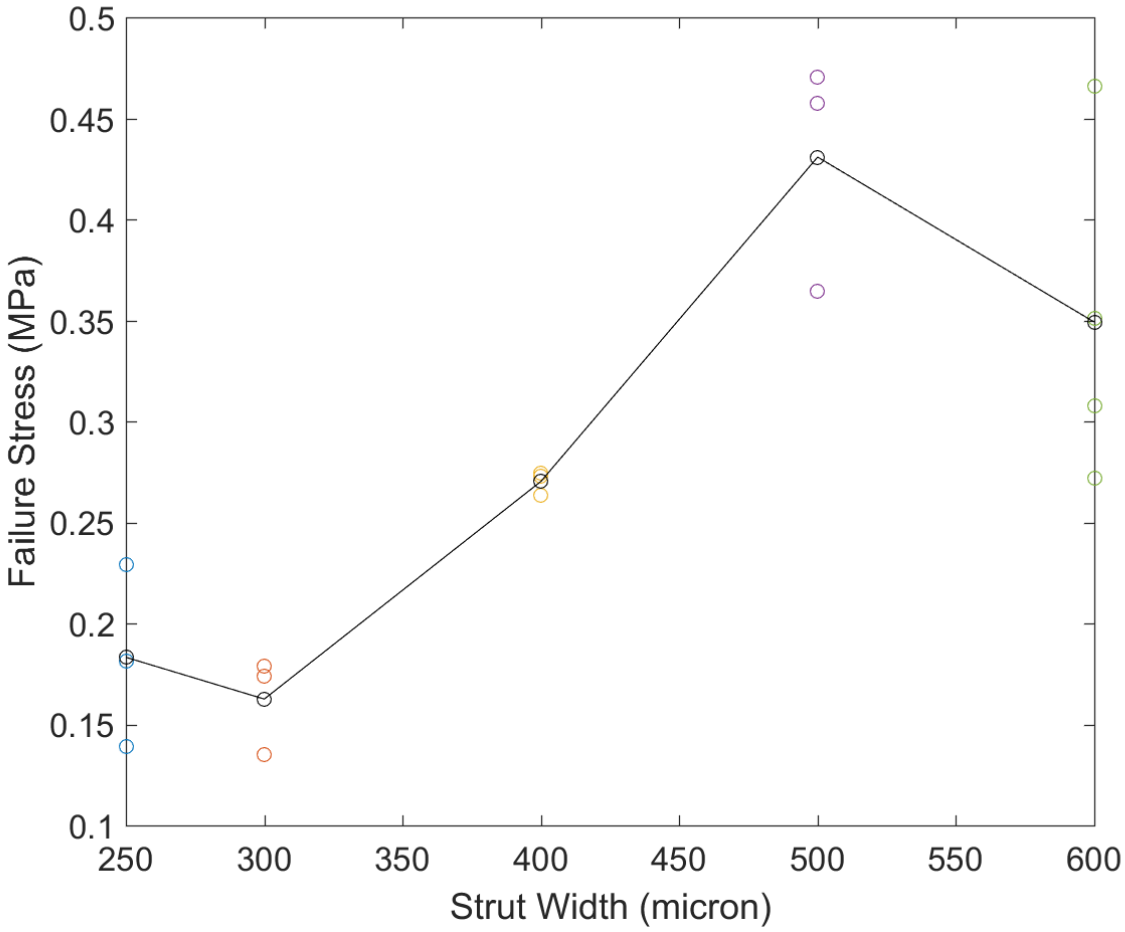

Figure 3.8: Plot shows compressive ultimate strength for equivalent relative density cuboctahedral lattices with various strut lengths, each 10 voxels per side. Black data points and line show the average value for that strut width.

Experimental Fracture Toughness Testing

Because the size of cellular solid specimens for a constant strut thickness increases as relative density decreases, lower relative density specimens can easily be twice the size of solid fracture specimens, though without an accompanying increase in fracture load. Accordingly, a custom clevis was designed to test the span of specimen sizes (Figure 3.9). This is a scaled version of the clevis design of ASTM E399, with a difference in the placement and size of the loading pin hole. This hole is sized to accommodate the largest specimen size, while its spacing from bottom edge of the clevis is sized to accommodate the smallest specimen tested. Because the fracture loads associated with polymer cellular materials are very low, analysis showed the stiffness of this altered clevis to be more than sufficient. Hollow carbon fiber composite tubes were used as pins, in order to minimize pre-loading on the structure from the weight of the pins (typically solid steel for testing of solid c(t) specimens). Stiffness of the carbon fiber loading pins was designed to match that of traditional steel pins under loads typical for the toughest materials tested by ASTM E399.

The loading rate for each specimen size was adjusted so that each was tested at a K rate of 3.1 x 10^{-4} $MPa\sqrt{m}$. This ultra-low loading rate was selected due to the brittle nature of the material and expected failure loads an order of magnitude lower than estimated for the solid constituent material (see Equation 3.1). Mode 1 fracture toughness K_Q was calculated using the standard calculation for compact tension specimens

$$K_Q = \frac{P_Q}{B\sqrt{W}} * f\left(\frac{a}{W}\right) \tag{3.3}$$

where a is the crack length, W is the specimen width, B is the specimen thickness, P_Q is the maximum load before crack propagation, and

$$f\left(\frac{a}{w}\right) = \frac{(2+\frac{a}{W})[0.886 + 4.64\frac{a}{W} - 13.32\frac{a}{W}^2 + 14.72\frac{a}{W}^3 - 5.6\frac{a}{W}^4]}{\left(1-\frac{a}{W}\right)^{3/2}} \tag{3.4}$$

For $a/W = 0.5$ used in this study, $f(a/W)$ evaluates to 9.66. As previously discussed, the function $f(a/W)$ was derived for continuum materials. Because the smallest characteristic dimension of the compact tension specimen is 10 voxels in length, a resolution at which modulus performance is well converged [14], we expect that this approximates the stress intensity factor well, for cellular materials at this scale. This assumption was tested computationally using FEM in the second half of this work as part of a larger investigation on the validity of continuum solutions for lattice materials.

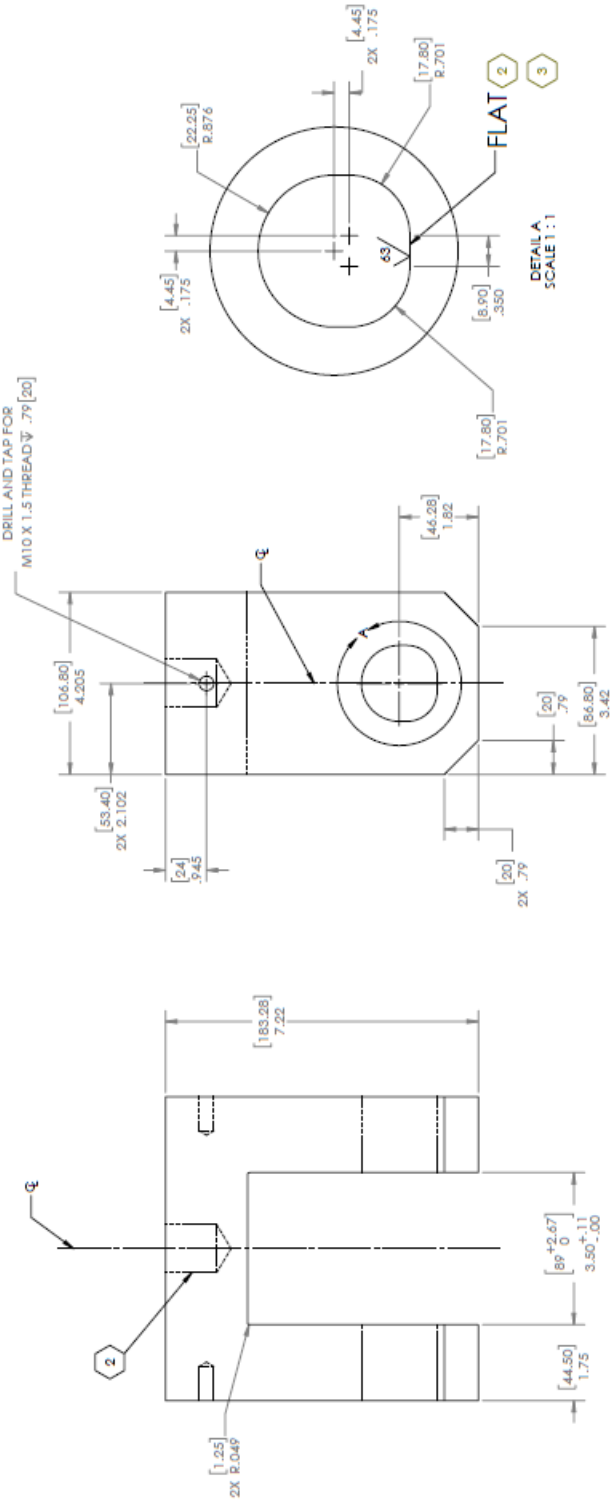

Figure 3.9: Clevis geometry.

Computational Methods

Finite element method (ABAQUS) was used to computationally approximate the normalized fracture toughness of the cuboct lattice across various relative densities and specimen sizes. Two different specimen geometries were tested: a center cracked plate loaded in tension and a side-cracked plate loaded in tension (Figure 3.10). For both specimen geometries, a unit force was applied to the top and bottom nodes of the plate. ABAQUS B31 elements (Euler Bernouli beams) with 1 element per strut provided sufficient resolution to capture behavior (further subdivisions did not affect results). Equation 3.1 can be rewritten as

$$\frac{K_{IC}}{\sigma_f\sqrt{\pi l}} = D\left(\frac{\rho}{\rho_s}\right)^d = \frac{Y\sigma_\infty\sqrt{\pi a_c}}{\sigma_f\sqrt{\pi l}} = \frac{Y\sigma_c\sqrt{a}}{\sigma_f\sqrt{l}} \tag{3.5}$$

where a_c is the critical crack length for fracture at a given far-field stress σ_∞, Y is a geometric factor, and σ_c is the critical far-field stress for fracture at a given crack length a. Since the maximum stress at the crack tip in the finite element simulations σ_{max} is equal to the rupture strength σ_f for crack propagation, substitution shows that

$$\frac{K_{IC}}{Y\sigma_f\sqrt{\pi a}} = \frac{\sigma_\infty}{\sigma_{max}} \tag{3.6}$$

By multiplying Equation 3.6 by $Y\sqrt{a/l}$, we recover the formulation of normalized fracture toughness in Equation 3.1, suitable for comparison with experimental results. Experimental results were compared to a side-cracked plate with 20 voxels wide, 20 voxels high, with a thickness of 10 voxels, and crack length a of 10 voxels. The geometry factor of an edge-cracked plate under uniform tension of $Y = 2.83$ was used from Tada, Paris, and Irwin's 'The Analysis of Cracks Handbook' [34]. It should be noted that Tada sources the polynomial expression to calculate Y across various a/W values for a side crack plate from Brown, who though he had a typo in his expression, first proposed the function. Brown's function was a least-squares regression of work by Gross, Strawley, and Brown [15] using the boundary collocation method, which was the same method used by Strawley [33] to calculate the f(a/W) expression given in the ASTM E399 standard for compact tension specimens [4]. The side-cracked plate geometry was also used to estimate the validity of the assumption of convergence to continuum behavior at $a/p = 10$ and the thickness necessary to achieve plane strain results. It should be noted that by applying a force instead of a displacement field, this method does not presume a particular asymptotic strain field ahead of the crack tip, which has recently been shown in 2D materials to be geometry dependent [35].

To interrogate the accuracy of the continuum geometry factor for a side-cracked plate of cuboctahedral lattice, side-cracked plate results were compared to those for a semi-infinite center-cracked plate. For a semi-infinite center-cracked plate, the theoretical geometry factor is 1. Therefore, to investigate the error associated with the continuum side-cracked plate geometry factor, the size of the center-cracked specimen was increased until a converged value of normalized fracture toughness was reached, implying an effectively semi-infinite

plate. Using the assumption that the fracture toughness of a center-cracked semi-infinite plate should be the same as that for a side-cracked plate, center-cracked results were used to approximate the geometry factor for a side-cracked plate of the same relative density and a/p.

The effects of specimen geometry and resolution were investigated for a side-cracked plate by varying the resolution a/p and the size of crack size relative to the specimen size, a/W, while maintaining approximately equal relative width, height, and thickness.

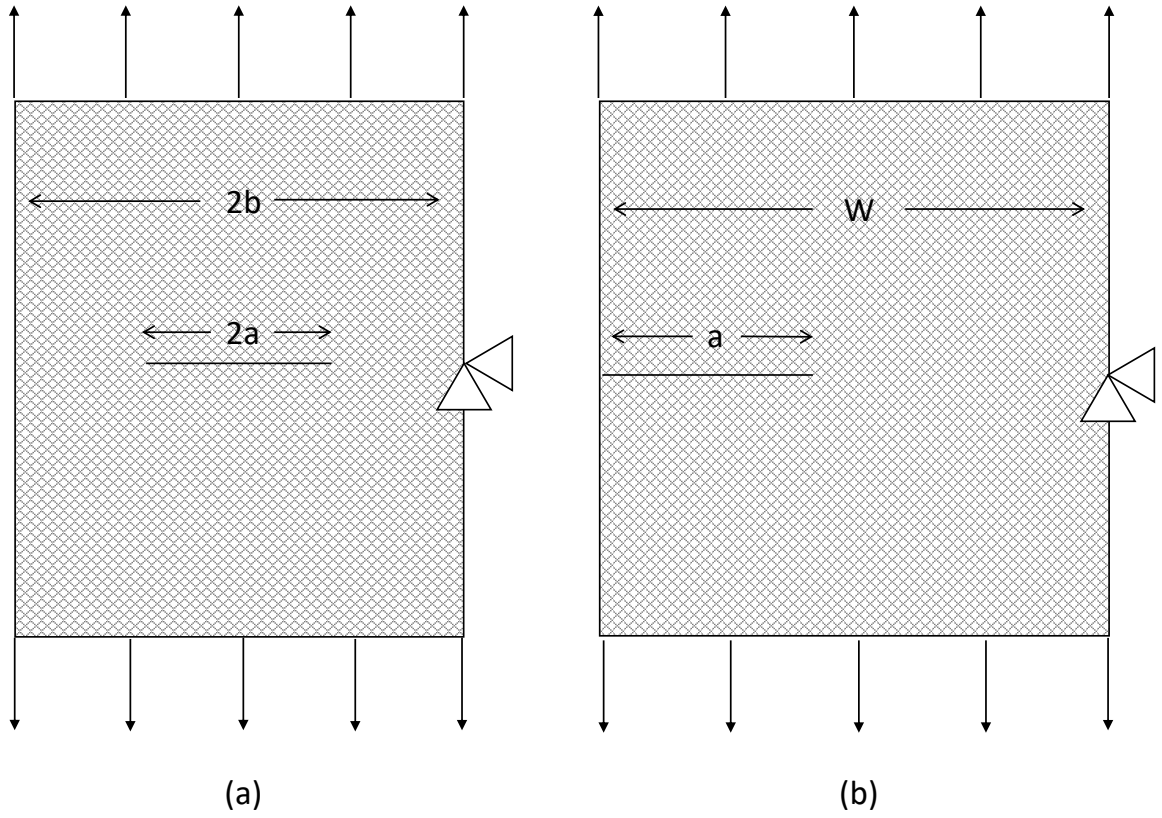

Figure 3.10: ABAQUS specimen diagrams for (a) center-cracked plate and (b) side-cracked plate.

3.3 Results and Discussion

Experimental fracture behavior was brittle in nature, with sudden catastrophic crack propagation (Figure 3.11), as expected from this type of polymer. All specimens satisfied Linear Elastic Fracture Mechanics plane-strain validity criterion, such that $B > 2.5(K_c/\sigma_y)^2$,

noting that due to the brittle nature of the material, $\sigma_u = \sigma_y$. Experimental results demonstrated linear scaling with relative density (Figure 3.13), outperforming stochastic foams and honeycombs. Interestingly, the results indicate that cuboct was able to match the scaling performance of the octet lattice despite having smaller lattice connectivity (8 vs. 12).

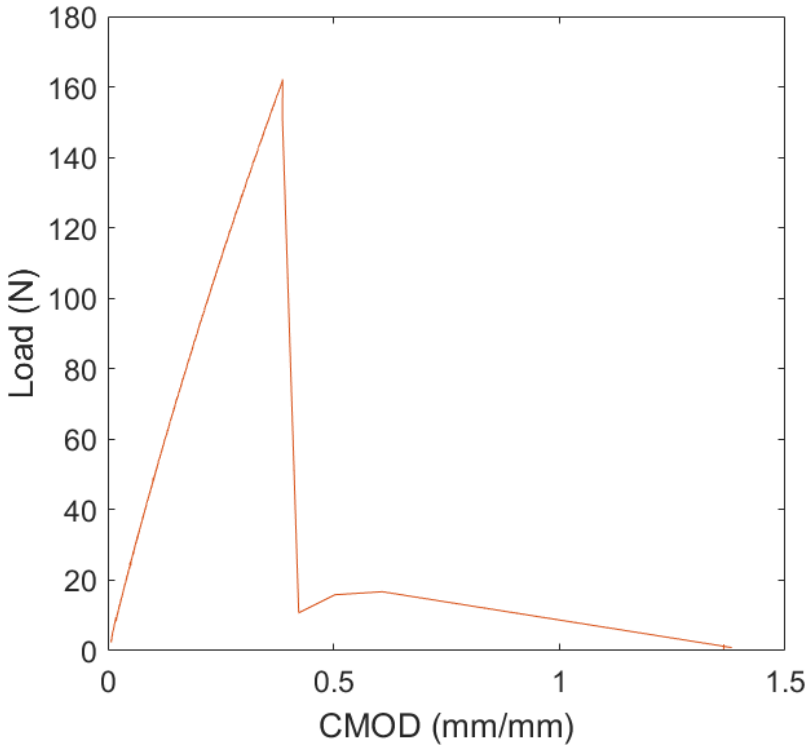

Figure 3.11: A typical load versus crack mouth opening displacement curve for a 4.81mm pitch (0.1 relative density) lattice compact tension specimen, demonstrating brittle behavior.

Results from ABAQUS simulations of a side-cracked plate with the same a/p and thickness also showed linear scaling of normalized fracture toughness with relative density (Figure 3.13). Computational investigation of the specimen resolution, a/l, on the value of the normalized fracture toughness for $a/W = 0.5$ is shown in 3.14. The normalized fracture toughness nears convergence at a/l = 20, but at a/l=10, the difference between the two is less than 5%. We expected that such differences are well within expect experimental variation measured in this study, and conclude that the chosen experimental sample size should well approximate converged behavior. Importantly, since all specimen relative dimensions were held constant, we can expect any variation to have minimal effect on scaling results. The trend of K_{norm} increasing with increasing resolution is opposite that observed for octet in [25], which observed an over-estimation of fracture toughness at lower resolution. This may be explained by the increase in strength and stiffness of the cuboct lattice when with

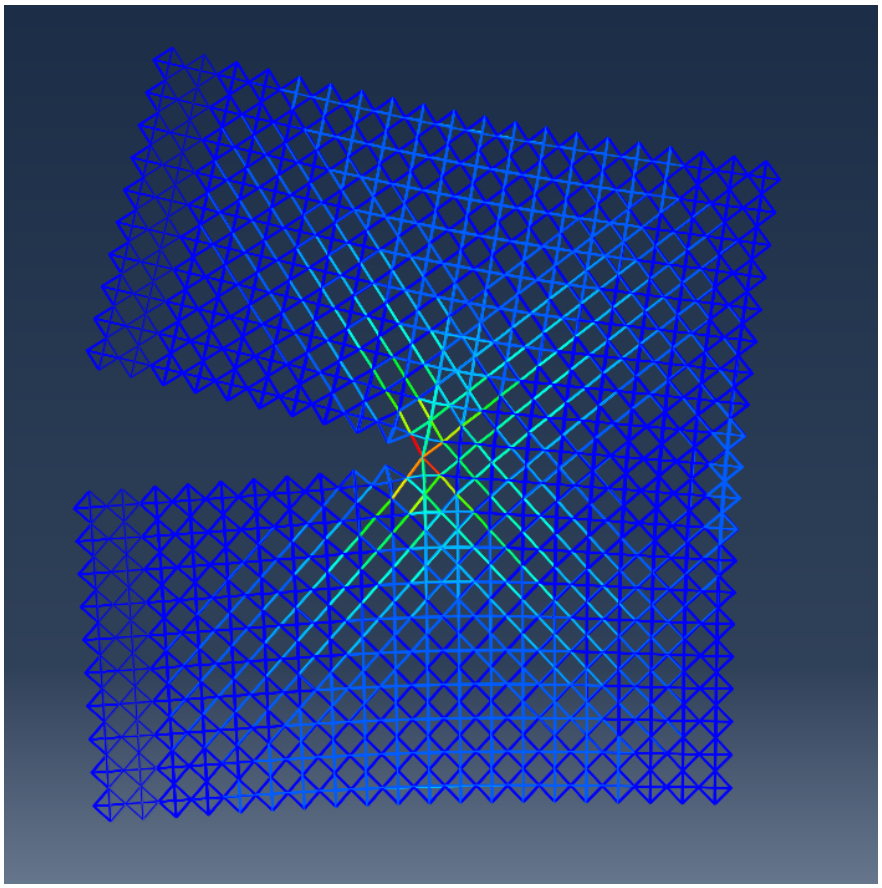

Figure 3.12: Visualization of simulated stress field ahead of the crack tip for a simulated 0.01 relative density, edge-cracked plate specimen.

increasing lattice resolution (though reasonable convergence was observed by 4 voxels per characteristic length) [14].

This effect of increasing resolution on bulk lattice behavior due to increasing constraint also explains the behavior as the thickness of a side-cracked specimen is increased. Figure 3.15 shows the effect of increasing voxel thickness on K_{norm} for a side-cracked plate. Distinct behavior is observed for thickness 3 voxels and below, regardless of the resolution of width and height of the plate. This transition to a different behavioral regime with two or more fully constrained interior voxels along the crack front is consistent with convergence behavior and deformation modes observed in previous studies of cuboct [14]. Importantly, these results show that plane strain can take on a more complicated meaning for lattice materials, even though the concept of designing a specimen with behavior dominated by fully constrained material through the thickness of the crack front remains unchanged. Plane strain for lattices must be understood not only as a limit on the bounding thickness of the specimen, but also on the number of voxels through the thickness necessary for constrained behavior. Additionally, and in violation of continuum conventions, Figure 3.15 suggests that plane-strain behavior

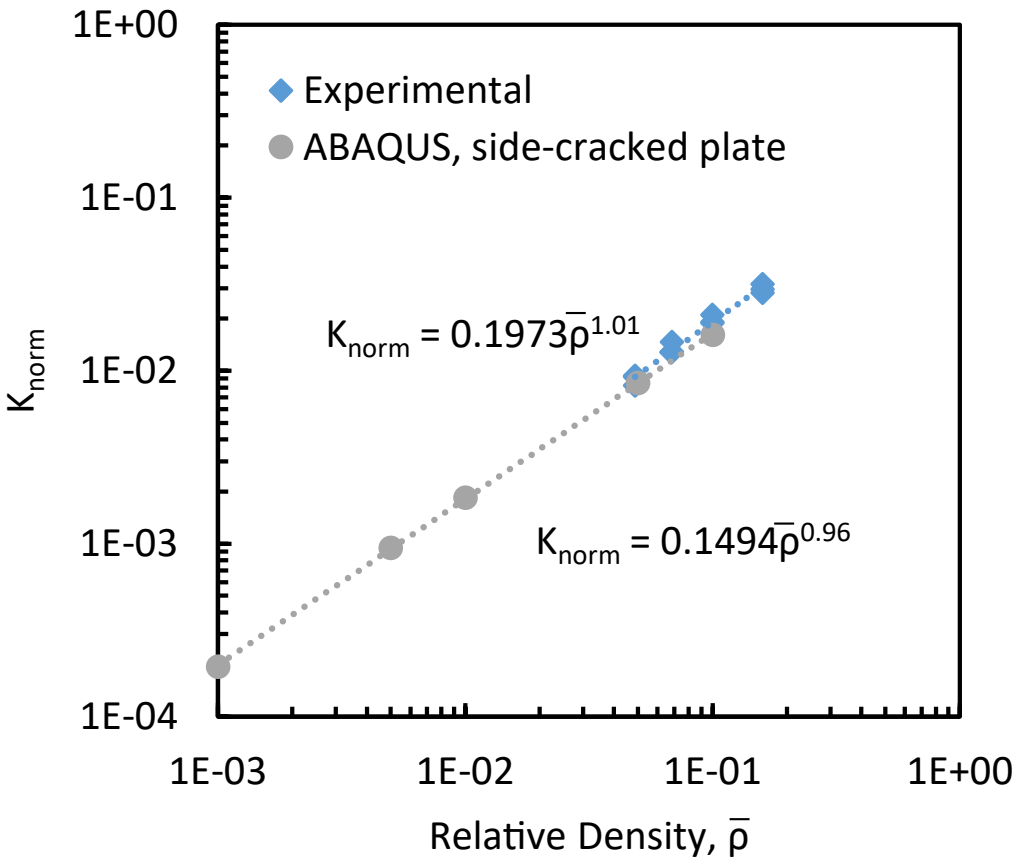

Figure 3.13: Computational and experimental results, both showing approximately linear scaling of normalized fracture toughness with relative density. ABAQUS simulations were for a side-cracked plate under uniform tension, a=10 voxels, thickness=10 voxels, width=height=20 voxels, and used the geometry factor given by Tada, Paris, and Irwin [34](Y=2.83) are shown.

may not always be assumed to be a conservative toughness value for all lattices (even though total variation between NB=1 and NB=a is less than 10% for cuboct for both resolutions studied).

While experimental and simulation scaling results agree well, they show a 1.3x disparity in linear scaling factor, D (Figure 3.13). Several factors may have contributed to this. The value of K_{norm} is very sensitive to the value of σ_f. Weaker than expected material strength due to printer variation would lead to an over-estimation of the normalized fracture toughness. To give a conservative value for K_{norm}, the experimental data was normalized by the ultimate strength of the material in the x-y plane, 45MPa. If the strength is dominated by the yield strengths or fracture strength of the z direction of 30 MPa, the experimental values of K_{norm}

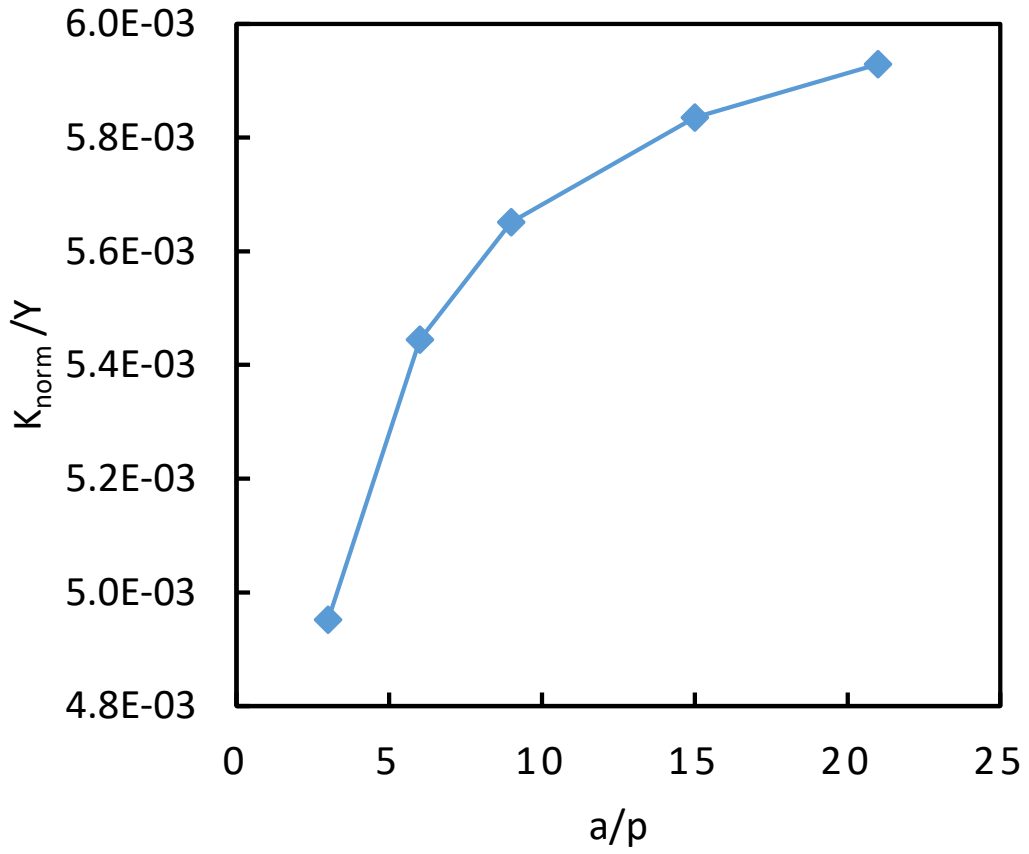

Figure 3.14: Convergence of K_{norm}/Y values for a side-cracked plate specimen in tension, with width and height $2a$ and thickness a ($a/W = 0.5$) for cuboct with a relative density of 0.1.

would be shifted even higher (leading to an almost 2x disparity in linear scaling factor). Additionally, the ABAQUS model used ideal node-to-node strut lengths. Smaller than ideal effective strut length present in the physical model due to the finite volume of the node would also contribute to an over-estimation of K_{norm}. As will be shown later, there is also reason to believe that the continuum geometry factors derived for both a compact tension specimen and side-cracked plate may not be equally accurate for the cuboct lattice.

Comparing ABAQUS simulations of a semi-infinite semi-cracked plate and the side-cracked plate provided an estimation of the accuracy of continuum stress concentration factors and the sensitivity of specimen geometry. Figure 3.16 shows the value K_{norm} for a center-cracked plate in tension with $a = 10$, thickness $B = 20$ and increasing plate size ($2b$). By $2b = 110$, results show a less than 1% variation from increasing the plate size. Taking this size as converged, the effect of plate thickness was investigated. Figure 3.17 shows that the

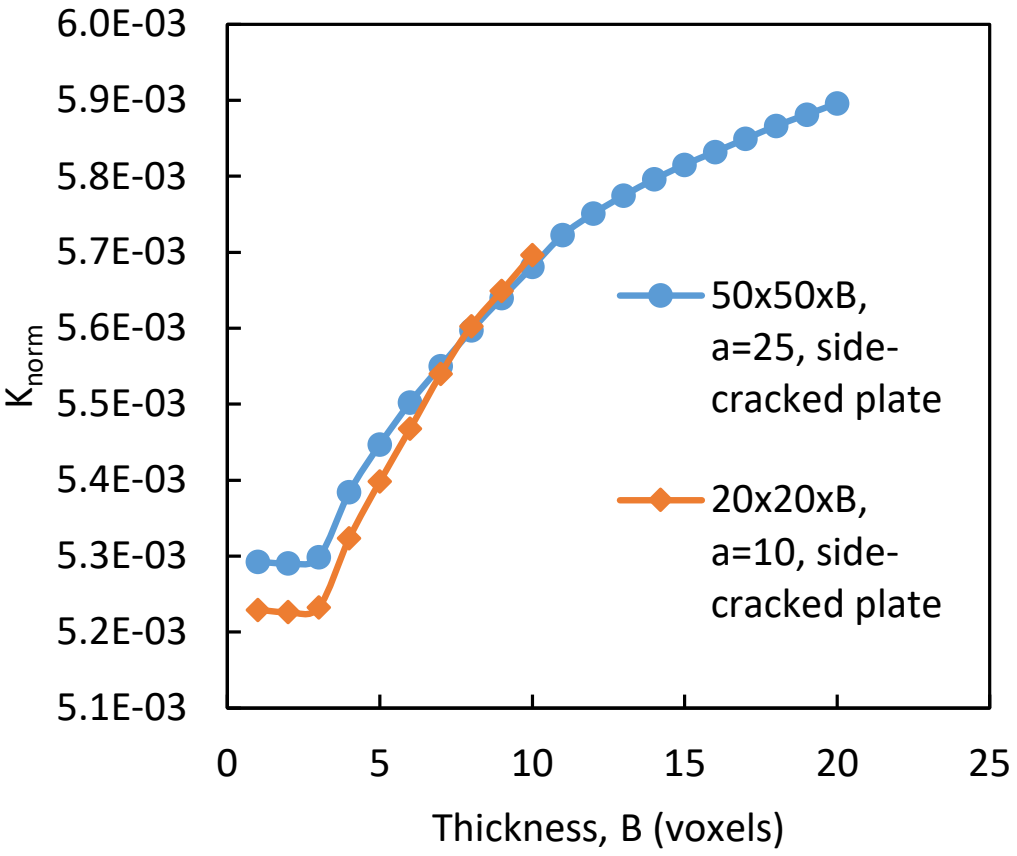

Figure 3.15: ABAQUS results for a 0.1 relative density cuboct lattice side-cracked specimen with width 2a, for various thicknesses.

relationship between K_{norm} and plate thickness is not monotonic. For the relative density sweep, we choose a thickness of 10 voxels because it was relevant for comparison to experiments, was relatively converged, and differed less than 5 % from higher values. The results of that relative density sweep are shown in Figure 3.18 and compared to the results for the side-cracked plate with no geometry correction. From this, we estimate that the appropriate geometry correction factor for cuboct with $a/p = 10$ and thickness 10 to be 3.2, 1.13 times larger than the continuum value 2.83 from Tada, Paris, and Irwin [34]. At this time, we cannot definitively say whether similar discrepancies contributed to the difference in linear scaling factor between experiment and simulation (Figure 3.13) because continuum geometry factors for both the compact tension specimen and the side cracked plate were calculated using the same methodology. However, it does highlight how both of these factors could be introducing at least 10% errors into both the experimental and computational measurement of lattice fracture toughness for comparison with continuum materials. The predicted error

associated with the continuum geometry factor for the compact tension specimen remains uncharacterized, and shall constitute future work.

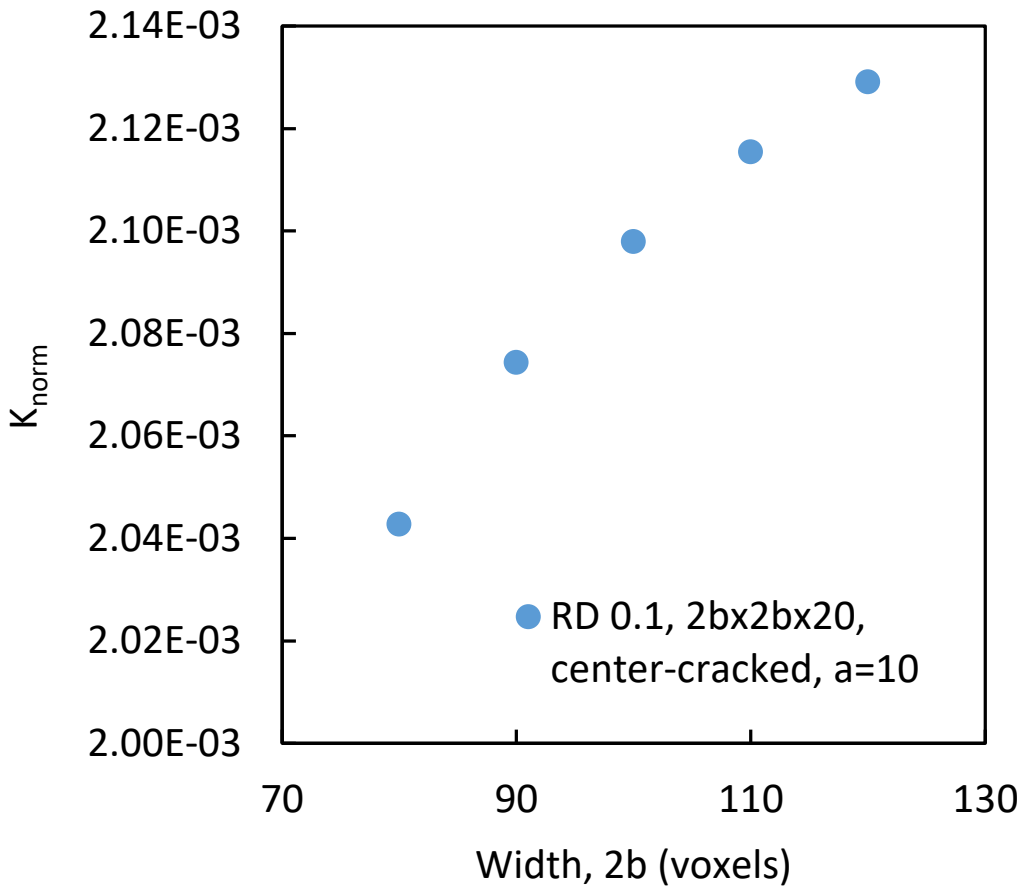

Figure 3.16: Size sweep for center-cracked specimen with $a = 10$ and thickness $B = 20$. As $2b$ approaches infinity, the geometry factor Y approaches 1.

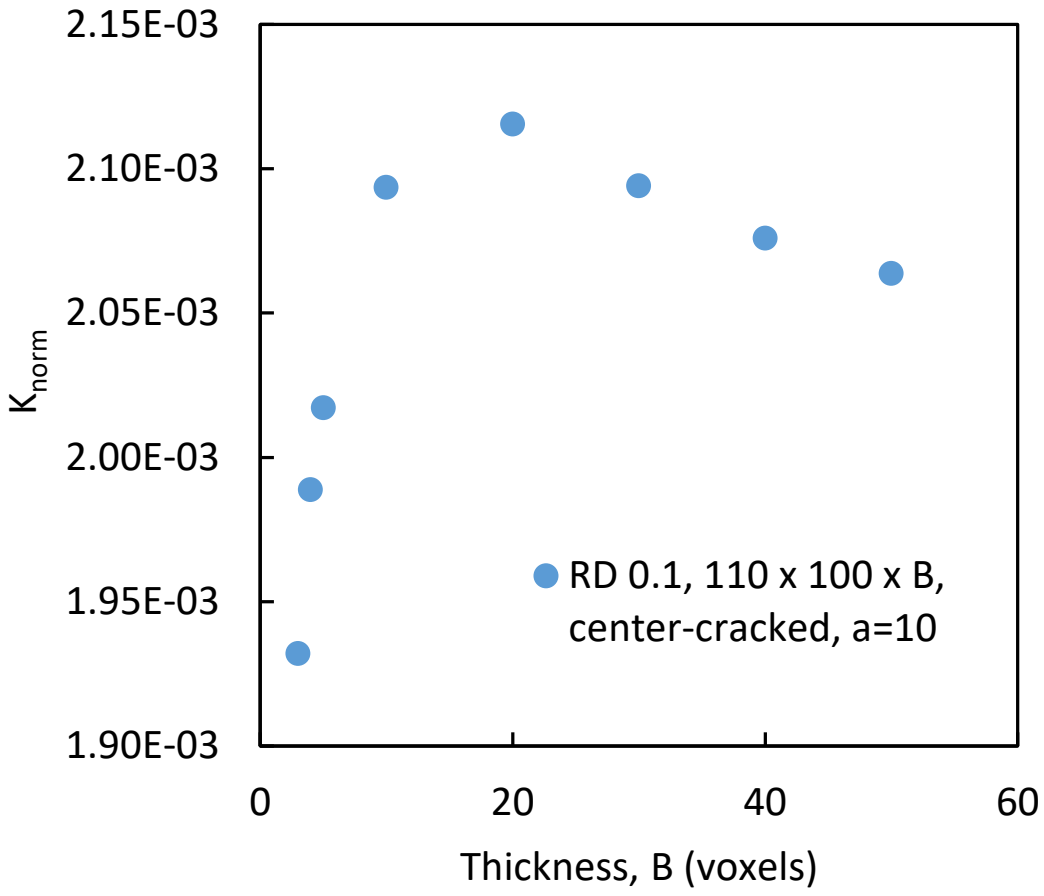

Figure 3.17: Thickness sweep for a 110x110xB center-cracked specimen with $a = 10$.

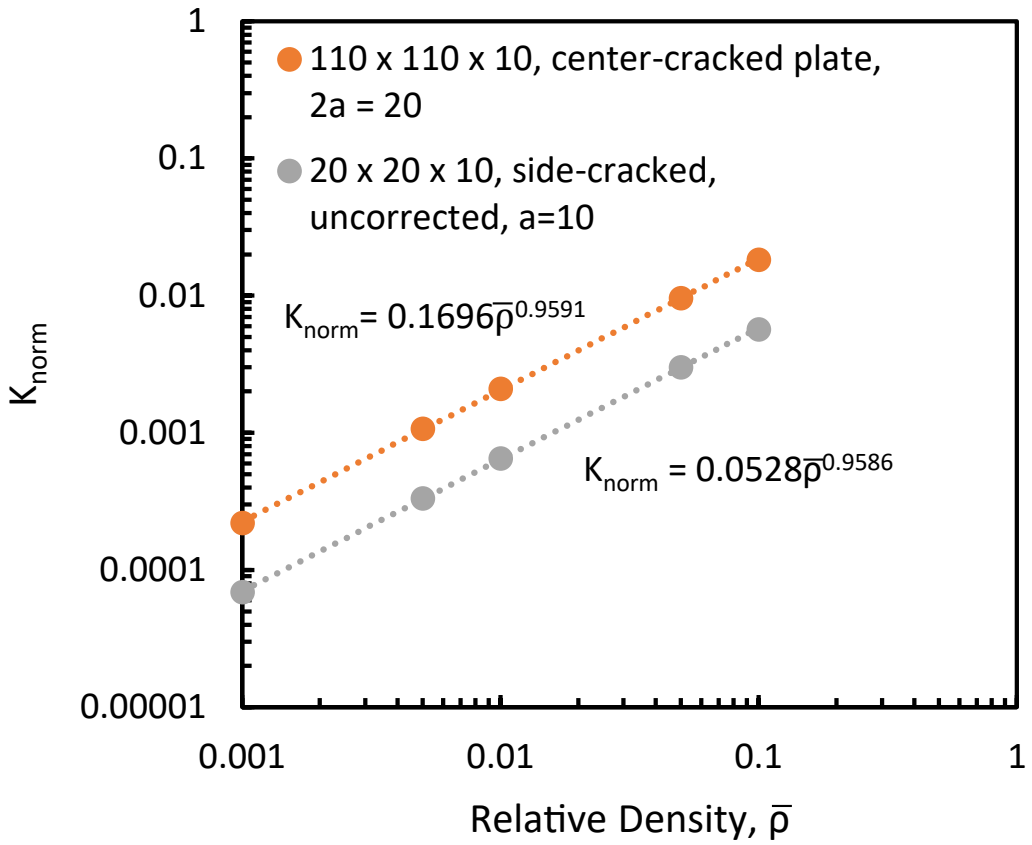

Figure 3.18: Relative density sweep for a 110x110x10 center-cracked specimen ($a = 10$), compared to results for a 20x20x10 side-cracked plate ($a = 10$) with no geometry correction factor.

3.4 Conclusions and Future Work

This study used computational and experimental methods to investigate the brittle fracture behavior of the cuboctahedral lattice and studied the lattice at a higher lattice resolution a/p than many previous studies to more closely approximate continuum behavior. A compact tension specimen for lattice materials was designed, manufactured using 3D printing, and tested. Both experimental and computational methods demonstrated linear scaling of fracture toughness with relative density. Disparity between linear scaling factors from ABAQUS and experimental results is attributed to material imperfections and non-ideal geometry. The sensitivity of the linear scaling factor to experimental factors such as material and effective strut length should caution researchers about the ability of simulation to predict the absolute magnitude of lattice fracture toughness. Additionally, computational investigation into the validity of the continuum geometry factors embedded in both experimental and computational procedures showed that these factors may not be as accurate for lattice materials. Specifically, computational results for cuboct predicted a more than 10% error from the continuum geometry factor at a relative density of 0.1, $a/W = 0.5$, and $a/P = 10$. Future work is necessary to fully characterize the appropriate geometry factor for various specimen geometries and relative densities. Additionally, the geometry factor is known to be less accurate at lower lattice resolutions a/P that are still relevant for various applications, and should be further characterized at all resolution scales that are likely to arise in practice. Results showing divergence from trends observed in the fracture of octet [25] highlight the critical need to perform geometry specific validation of lattice fracture characteristics.

Chapter 4

Toughing Lattices with He-Hedgepeth Criterion

4.1 Introduction

One of the primary advantages of lattice materials is the tunability of their strength and stiffness. By carefully selecting constituent material and lattice architectures, many different responses can be engineered, optimizing for energy absorption, stiffness, strength, and other properties.

We seek to extend this tunability to be able to design for fracture toughness. As discussed in the previous section, fracture toughness is a key enabling property for the practical implementation of these materials into safety critical applications. Continuum materials possess many strategies for enhancing fracture toughness [30]. We hypothesize that many of these could be applied to lattice materials to enhance their fracture toughness.

This chapter investigates the incorporation of heterogeneities into lattices to cause crack deflection, desiging lattice materials with reinforcement phases to increase fracture toughness. To design the reinforcement phase, we seek use the He-Hedgepeth framework to predict the modulus mismatch necessary to cause crack deflection at the interface between the matrix lattice and reinforcement lattice.

Cellular Material Basics

The extension of the He-Hedgepeth framework to lattice material relies upon an understanding of their properties in the context of cellular materials, which for the sake of definition of terms, is repeated here from Chapter 1. Pioneering work by Ashby and Gibson showed that material properties of cellular materials can be successfully predicted based on the geometry of the cell, the base material, and the relative density [3, 13]. This derivation utilizes the fact that the relative modulus of a lattice material $\bar{E}$ is given by

$$\bar{E} = \frac{E_L}{E_s} = A\bar{\rho}^a$$

where E_L is the modulus of the lattice, E_s is the modulus of the solid constituent material, $\bar{\rho}$ is the relative density, and A and a are constants. If one wishes to design a heterogeneous lattice material, one can achieve phases of differing stiffnesses by changing the geometry, material, relative density, or any combination of these, though interface requirements place restrictions on what geometries may be compatible. In this study, only the relative density is changed between phases in the heterogeneous lattice.

Similar to the elastic modulus, the Mode 1 fracture toughness of a lattice material K_1 was found to scale with relative density such that

$$K_1 = D\bar{\rho}^d$$

where D is a function of the rupture strength of the material and the crack length. The exponents a and d are both geometry dependent, whereas A and D are dependent upon both geometry and material. This derivation utilizes the cuboctahedral lattice geometry (vertex connected octahedra), hereafter referred to as cuboct, as a prototypical geometry. The values of a and d for cuboct have been determined as 1.5 and 1 respectively from experimental study [6].

He-Hedgepeth Framework

The He-Hedgepeth framework [17] predicts whether a crack moving from material 2 into material 1 will penetrate the interface, or arrest or delaminate at the interface (Figure 4.1). It is extensively used in the design of composite materials [1, 5] and also to explain mechanistic fracture of natural composites like bone [43]. It's prediction of crack penetration depends on Dundur's parameter α, which characterizes the elastic modulus mismatch between two materials 1 and 2 such that $\alpha = (E_1 - E_2)/(E_1 + E_2)$ (E_i = plane strain tensile modulus), and the ratio of the interface toughness to the toughness of material 2 (expressed as strain energy release rates G_{int} and G_2 respectively.

The impinging crack is not expected to penetrate the interface if

$$G_{int}/G_1 < G_d/G_p$$

where G_d is the energy release rate of the crack deflection and G_p is the energy release rate of the crack penetration.

Expressions for G_p and G_d come from continuum calculations taken from He-Hedgepeth criterion of the energy release rates for elastic and isotropic materials with shear modulus μ_i and Poisson's ration ν_i. Plane strain, traction boundary value problems are considered that depend on the Dundur's parameters

$$\alpha = \frac{\mu_1(1-\nu_2) - \mu_2(1-\nu_1)}{\mu_1(1-\nu_2) + \mu_2(1-\nu_1)} = \frac{E_1 - E_2}{E_1 + E_2}$$

$$2\beta = \frac{\mu_1(1-2\nu_2) - \mu_2(1-2\nu_1)}{\mu_1(1-\nu_2) + \mu_2(1-\nu_1)}$$

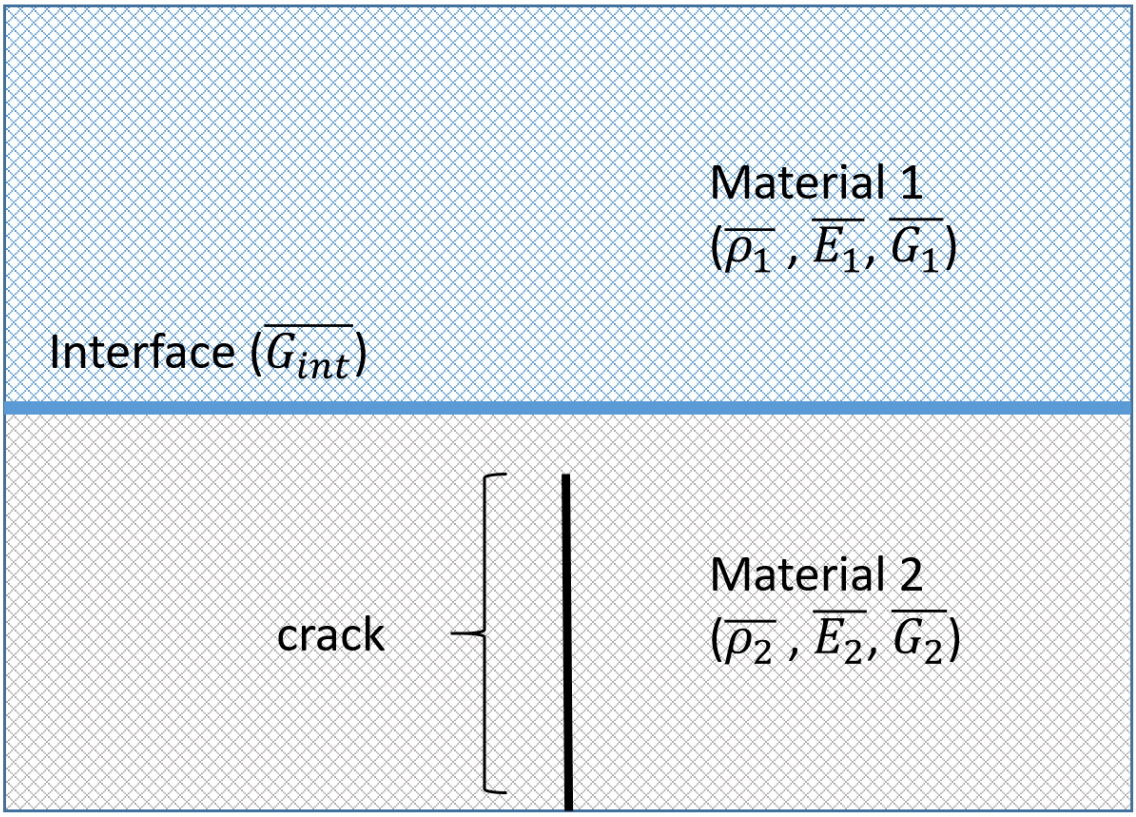

Figure 4.1: He-Hedgepeth bimaterial.

where E_i are the plane strain tensile moduli.

The He-Hedgepeth framework gives the following expression for the relative tendency of a crack to be deflected by the interface or to pass through it:

$$G_d/G_p = \frac{1-\beta^2}{1-\alpha}\left[\frac{|d_1|^2 + |e|^2 + 2R_e(de)}{c^2}\right]$$

where d_1 and e are dimensionless complex valued functions of α and β and c is a dimensionless real-valued function of α and β from the stress intensity factor $K_1 = c(\alpha, \beta)k_1 a^{0.5-\lambda}$.

This analysis does not resolve the He-Hedgepeth expression for G_d/G_p, but rather seeks to predict G_{int}/G_1 and compare this to the He-Hedgepeth solution. Note that in Hedgepeth's original solution, β is assumed to be zero and have little affect.

4.2 Extension to Lattice Materials

We wish to extend the He-Hedgepeth framework to lattice materials to design rip-stop lattice solids by introducing crack-deflection heterogeneities into the lattice structure. In this study, the meaning of heterogeneous lattice is restricted to differences in relative density. Though narrow in the scheme of all possible lattice heterogeneities, which could include geometry and material, restricting the change to relative density is a realistic restriction for many monolithic lattice manufacturing processes such as 3D printing. We will also show that this restriction allows for elegant simplification of the criterion. To approximate the He-Hedgepeth criterion for a heterogeneous cuboct lattice, the following is assumed:

1. The toughness of the interface is approximately the toughness of the lower-density lattice i.e, $G_{int} = G_2$, assumed as such because the interface strength will be limited by the strength of the most slender struts at the interface (those of the lowest relative density lattice).

2. The strain energy release rate G and the mode 1 fracture toughness K of are proportional and scale with the same power with relative density.

3. The cuboct lattice shows linear scaling with relative density for fracture toughness, i.e. $d = 1$

4. The relative modulus $\bar{E} = E_{lattice}/E_{solid}$ of the cuboct lattice scales with the relative density to a factor of 1.5, i.e., $a = 1.5$

5. The plane strain tensile modulus is equivalent to the plane strain compressive modulus (experimental results suggests this is true) i.e., $E_{ten} = E_{comp}$

6. E_i is plane strain modulus

Because the relative modulus and fracture toughness of a lattice with a given material and geometry are dependent upon the relative density, it should be possible to reduce the deflection condition to a critical mismatch of relative density.

For this example, only the relative density of the reinforcement phase changes, not the geometry or the material. Therefore, the know that the Poisson ratios of each phase will be equivalent, since the Poisson ratio is not relative density dependent [13]. Therefore, since $\nu_1 = \nu_2 = \nu$ we can write

$$2\beta = \frac{\mu_1(1-2\nu) - \mu_2(1-2\nu)}{\mu_1(1-\nu) + \mu_2(1-\nu)} = \frac{(\mu_1 - \mu_2)(1-2\nu)}{(\mu_1 + \mu_2)(1-\nu)}$$

However, Schmauder notes in "Correlation between Dundur's Parameters and Elastic Constants' [32, Eq.11] that for $\nu_1 = \nu_2 = 1/3$, this further simplifies for plane strain to

$$\beta = \alpha/4$$

Since we know that the relative modulus of a given lattice $\bar{E}$ is given by

$$\bar{E} = \frac{E_L}{E_s} = A\bar{\rho}^a$$

where E_L is the modulus of the lattice, E_s is the modulus of the solid constituent material, $\bar{\rho}$ is the relative density, and A and a are constants, we can substitute this into the expression for α, we get the following:

$$\alpha = \frac{E_s A\bar{\rho_1}^a - E_s A\bar{\rho_2}^a}{E_s A\bar{\rho_1}^a + E_s A\bar{\rho_2}^a} = \frac{\bar{\rho_1}^a - \bar{\rho_2}^a}{\bar{\rho_1}^a + \bar{\rho_2}^a}$$

If we rewrite this expression for α using the ratio of relative densities $r = \bar{\rho_2}/\bar{\rho_1}$,

$$\alpha = \frac{1 - r^a}{1 + r^a}$$

and it's inverse

$$r = \sqrt[a]{\frac{1-\alpha}{1+\alpha}}$$

Similarly, the mode 1 fracture toughness K_1 of lattices can be written as

$$K_1 = D\bar{\rho}^d$$

Since we are assuming that the energy release rate G is proportional to the mode 1 fracture toughness of the lattices, we can write

$$\frac{G_{int}}{G_1} = \frac{D\bar{\rho_2}^d}{D\bar{\rho_1}^d} = r^d$$

When combined with the expression for α in terms of ρ, this leaves us with a tidy statement for the problem of designing lattice relative density mismatches to produce crack deflection. We are looking for a relative density ratio r such that

$$\frac{G_{int}}{G_1} = r^d < G_d/G_p = f(\alpha, \beta) = f(r)$$

as calculated by He-Hedgepeth. This can also be written as

$$\frac{G_{int}}{G_1} = \left(\frac{1-\alpha}{1+\alpha}\right)^{d/a} < G_d/G_p$$

We solve this inequality graphically in Figure 4.2 for cuboct, with a = 1.5 and d= 1.

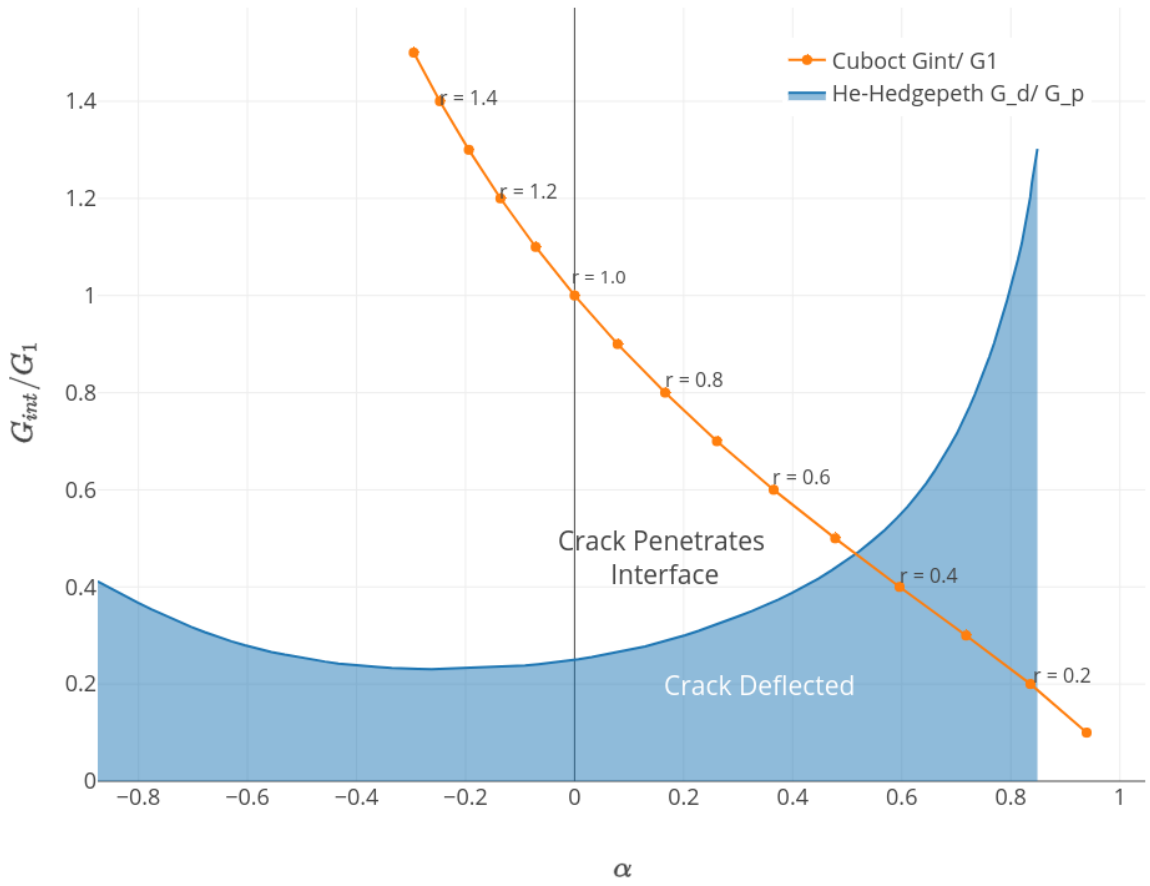

Figure 4.2: He-Hedgepeth curve showing regimes of predicted crack penetration and deflection. The orange curve shows the predicted values for cuboct, with various values of r labeled. It can be seen that for r < 0.45, crack deflection is predicted.

Preliminary Experimental Validation

Preliminary experiments were conducted to validate this theoretical framework. Compact tension cuboctahedral fracture specimens were printed using a ProJet 3600 polyjet printer, using the same methodology described in Chapter 3. The specimens were patterned such that every other voxel was a different relative density (and strut width), except for the homogeneous specimen included for comparison. All specimens were approximately the same over-all relative density. For each specimen, the first voxel ahead of the crack tip was the voxel with the smaller relative density and strut width.

Characteristic load-displacement curves for each heterogeneous specimen from preliminary fracture experiments can be seen in Figure 4.3. As predicted by theory, the homo-

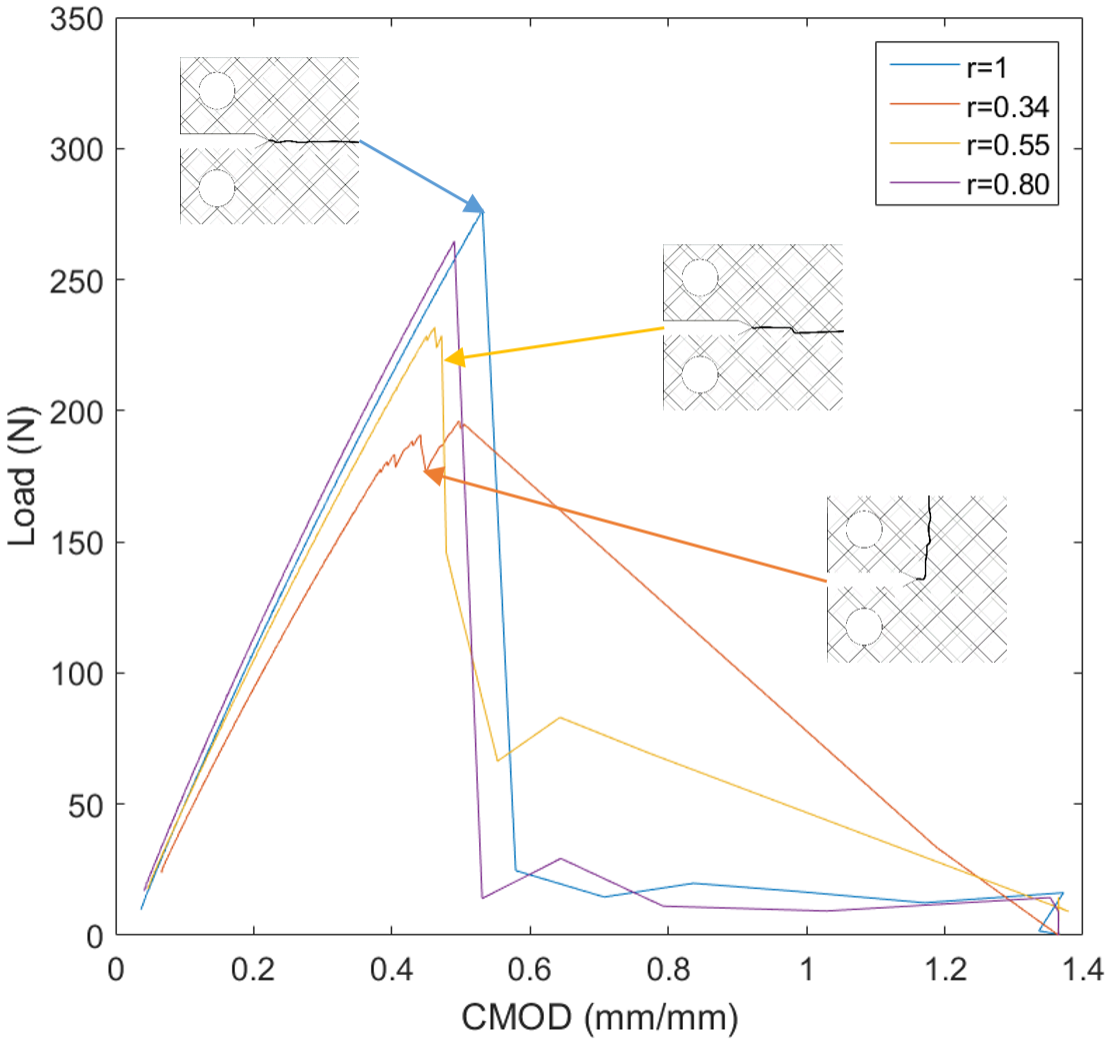

Figure 4.3: Characteristic load-displacement curves for each heterogeneous specimen from preliminary fracture experiments. As predicted by theory, the r= 1 and r=0.796 specimens showed no crack deflection. The transition case r=0.550 showed minimal evidence of crack deflection, while the most mismatched case r = 0.340 showed complete crack deflection.

geneous r= 1 and (SW650SW750) r=0.796 specimens (strut widths 650 micron and 750 micron) showed no crack deflection. The transition case r=0.550 (strut widths of 600 micron and 800 micron) showed minimal evidence of crack deflection, while the most mismatched case, r = 0.340 (strut widths 510micron and 860 micron), showed complete crack deflection. The increasingly lowered load for initiation of fracture is expected due to the decreased strut width of the voxel just ahead of the crack tip. Since the initiation of fracture is controlled

by the strength of the struts just ahead of the crack tip, the relative density of the voxel just ahead of the crack tip will always control the fracture initiation load. This is typical of brittle materials, which rely on extrinsic toughening mechanisms to extend their toughness after initial crack initiation [30].

4.3 Conclusions

The He-Hedgepeth crack deflection criterion for a heterogeneous lattice solid (single material, single geometry, multi-relative density) can be reduced to a critical relative density mismatch between the matrix and reinforcement phases, provided that the relative density scaling of the fracture toughness and modulus are known. This is extensible to any geometry. Experimental results demonstrate successful prediction of crack deflection, with mixed behavior occurring at r values close to transitions values. Future work will seek to extend this criterion to other lattice heterogeneities.

Chapter 5

Conclusion

This thesis focused on practical issues facing wide-scale use of lattice materials in large-scale, safety critical applications. At the heart of the issue of manufacturing lies the reality that 'if you can't make it, it doesn't matter'. For architected lattice materials to be interesting, they must be made available on the scale of material needed for high impact applications like aircraft. The demonstration of injection molded discrete lattice materials demonstrates this scalability on many levels. It shows that traditional mass manufacturing can be used to make geometrically complex unit cells, and design features can create a robust and repeatable lattice (alignment features, bolted connection). Perhaps most importantly, it demonstrated a key potential advantage of discrete lattice materials: repairability. When combined with reconfigurability, repairability dramatically extends the life-cycle of the material and multiplies the weight savings of lattice materials in space infrastructure applications.

However, use of lattice materials also relies on understanding of their damage mechanisms. Chapter 3 contributed to the nascent field of lattice fracture mechanics by characerizing the relative density scaling of fracture toughness for the cuboctahedral lattice. More critically, it called attention to the lack of understanding of geometry factors and K-calibration for 3D lattice geometries. This work should motivate increased attention by the field of understanding how to properly estimate the K-field ahead of a crack tip in a lattice and account for differences based on relative density, material, and geometry.

Many opportunities exist for designing tougher lattices. This thesis presented a criterion for prediction crack deflection in a lattice with heterogeneous relative density. But other methods may exist. There may be geometries that have crack-shielding mechanisms to relieve strain at the crack tip. Heterogeneities (material, relative density, geometry) may be included into the lattice to deflect cracks or absorb energy. Future work will involve continued investigation of these opportunities.

Bibliography

[1] G. Anthony, Ming Y. He, and John W. Hutchinson. "Interface debonding and fiber cracking in brittle matrix composites". In: *Journal of American Ceramic Society* 72.12 (1989), pp. 2300–2303.

[2] Steven M Arnold, David Cebon, and Mike Ashby. *Materials selection for aerospace*. Tech. rep. October. NASA, 2012, pp. 1–64. DOI: 10.1533/9780857095152.569. URL: http://linkinghub.elsevier.com/retrieve/pii/B978185573946850025X.

[3] M F Ashby. "The mechanical properties of cellular solids". In: *Metallurgical Transactions A* 14.9 (1983), pp. 1755–1769. ISSN: 0360-2133, 1543-1940. DOI: 10.1007/BF02645546. URL: http://link.springer.com/article/10.1007/BF02645546.

[4] ASTM International. *ASTM E399: Standard Test Method for Linear-Elastic Plane-Strain Fracture Toughness K1C of Metallic Material*. Tech. rep. 2013, pp. 1–33. DOI: 10.1520/E0399-12E03.2.

[5] H. C. Cao et al. "Effect of interfaces on the properties of fiber-reinforced ceramics". In: *Journal of the American Ceramic Society* 73.6 (1990), pp. 1691–1699. ISSN: 15512916.

[6] Kenneth C. Cheung and Neil Gershenfeld. "Reversibly assembled cellular composite materials". In: *Science* 341.September (2013), pp. 1219–1221. ISSN: 00104361. DOI: 10.1177/0892705714554493. URL: http://www.sciencemag.org/cgi/doi/10.1126/science.1240889.

[7] Brett G. Compton and Jennifer A. Lewis. "3D-printing of lightweight cellular composites". In: *Advanced Materials* 26.34 (2014), pp. 5930–5935. ISSN: 15214095. DOI: 10.1002/adma.201401804.

[8] V. S. Deshpande, M. F. Ashby, and N. A. Fleck. "Foam topology: Bending versus stretching dominated architectures". In: *Acta Materialia* 49.6 (2001), pp. 1035–1040. ISSN: 13596454. DOI: 10.1016/S1359-6454(00)00379-7.

[9] Liang Dong, Vikram Deshpande, and Haydn Wadley. "Mechanical response of Ti-6Al-4V octet-truss lattice structures". In: *International Journal of Solids and Structures* 60 (2015), pp. 107–124. ISSN: 00207683. DOI: 10.1016/j.ijsolstr.2015.02.020. URL: http://dx.doi.org/10.1016/j.ijsolstr.2015.02.020.

[10] Liang Dong and Haydn Wadley. "Mechanical properties of carbon fiber composite octet-truss lattice structures". In: *Composites Science and Technology* 119 (2015), pp. 26–33. ISSN: 02663538. DOI: 10.1016/j.compscitech.2015.09.022. URL: http://dx.doi.org/10.1016/j.compscitech.2015.09.022.

[11] Norman A. Fleck and XinMing Qiu. "The damage tolerance of elastic-brittle, two-dimensional isotropic lattices". In: *Journal of the Mechanics and Physics of Solids* 55.3 (2007), pp. 562–588. ISSN: 00225096. DOI: 10.1016/j.jmps.2006.08.004.

[12] Lorna J. Gibson. "Modelling the mechanical behavior of cellular materials". In: *Materials Science and Engineering: A* 110 (1989), pp. 1–36. ISSN: 09215093. DOI: 10.1016/0921-5093(89)90154-8.

[13] Lorna J. Gibson and Michael F. Ashby. *Cellular Solids: Structure and Properties*. 2nd. New York: Cambridge University Press, 1997.

[14] Christine E. Gregg, Joseph H. Kim, and Kenneth C. Cheung. "Ultra-light and scalable composite lattice materials". In: *Advanced Engineering Materials* 1800213 (2018), pp. 1–6. DOI: 10.1002/adem.201800213.

[15] Bernard Gross, John E. Srawley, and William F. Jr. Brown. *Stress-Intensity Factors for a Single-Edge-Notch Tension Specimen By Boundary Collocation of a Stress Function*. Tech. rep. Cleveland, Ohio: NASA, 1964, pp. 1–12.

[16] X. Edward Guo and Lorna J. Gibson. "Behavior of intact and damaged honeycombs: A finite element study". In: *International Journal of Mechanical Sciences* 41.1 (1999), pp. 85–105. ISSN: 00207403. DOI: 10.1016/S0020-7403(98)00037-X. URL: http://www.sciencedirect.com/science/article/pii/S002074039800037X.

[17] Ming-Yuan He and John W. Hutchinson. "Crack deflection at an interface between dissimilar elastic materials". In: *International Journal of Solids and Structures* 25.9 (1989), pp. 1053–1067.

[18] Han; Hu et al. "Ultralight and highly compressible graphene aerogels". In: *Advanced Materials* 25.15 (2013), pp. 2219–2223. ISSN: 09359648.

[19] J. S. Huang and Lorna J. Gibson. "Fracture toughness of brittle foams". In: *Acta Metallurgica Et Materialia* 39.7 (1991), pp. 1627–1636. ISSN: 09567151. DOI: 10.1016/0956-7151(91)90250-5.

[20] J. S. Huang and Lorna J. Gibson. "Fracture toughness of brittle honeycombs". In: *Acta Metallurgica et Materialia* 39.7 (1991), pp. 1617–1626. ISSN: 09567151. DOI: 10.1016/0956-7151(91)90249-Z.

[21] Bin Jiang et al. "Ultralight metal foams". In: *Scientific Reports* 5 (2015), p. 13825. ISSN: 2045-2322. DOI: 10.1038/srep13825. URL: http://www.nature.com/doifinder/10.1038/srep13825.

[22] Leonid Kucherov and Michael Ryvkin. "Fracture toughness of open-cell Kelvin foam". In: *International Journal of Solids and Structures* 51.2 (2014), pp. 440–448. ISSN: 00207683. DOI: 10.1016/j.ijsolstr.2013.10.015. URL: http://dx.doi.org/10.1016/j.ijsolstr.2013.10.015.

[23] Amitesh Maiti et al. "3D printed cellular solid outperforms traditional stochastic foam in long-term mechanical response". In: *Scientific Reports* 6.April (2016), p. 24871. ISSN: 2045-2322. DOI: 10.1038/srep24871. URL: http://www.nature.com/articles/srep24871.

[24] Lucas R Meza, Satyajit Das, and Julia R Greer. "Strong, lightweight, and recoverable three-dimensional ceramic nanolattices". In: *Science* 345.6202 (2014), pp. 1322–1326. ISSN: 0036-8075. DOI: 10.1126/science.1255908. URL: www.sciencemag.org/content/345/6202/1322/suppl/DC1.

[25] M.R. OMasta et al. "The fracture toughness of octet-truss lattices". In: *Journal of the Mechanics and Physics of Solids* 98.2017 (2017), pp. 271–289. ISSN: 00225096. DOI: 10.1016/j.jmps.2016.09.009. URL: http://linkinghub.elsevier.com/retrieve/pii/S0022509616302952%20http://dx.doi.org/10.1016/j.jmps.2016.09.009.

[26] Douglas T. Queheillalt and Haydn Wadley. "Cellular metal lattices with hollow trusses". In: *Acta Materialia* 53.2 (2005), pp. 303–313. ISSN: 13596454. DOI: 10.1016/j.actamat.2004.09.024.

[27] Ignacio Quintana Alonso and Norman A. Fleck. "Damage tolerance of an elastic-brittle diamond-celled honeycomb". In: *Scripta Materialia* 56.8 (2007), pp. 693–696. ISSN: 13596462. DOI: 10.1016/j.scriptamat.2006.12.027.

[28] Ignacio Quintana-Alonso et al. "The fracture toughness of a cordierite square lattice". In: *Acta Materialia* 58.1 (2010), pp. 201–207. ISSN: 13596454. DOI: 10.1016/j.actamat.2009.08.069. URL: http://dx.doi.org/10.1016/j.actamat.2009.08.069.

[29] M. G. Rashed et al. "Metallic microlattice materials: A current state of the art on manufacturing, mechanical properties and applications". In: *Materials and Design* 95 (2016), pp. 518–533. ISSN: 18734197. DOI: 10.1016/j.matdes.2016.01.146. URL: http://dx.doi.org/10.1016/j.matdes.2016.01.146.

[30] Robert O. Ritchie. "The conflicts between strength and toughness". In: *Nature Materials* 10.11 (2011), pp. 817–822. ISSN: 1476-1122. DOI: 10.1038/nmat3115. URL: http://www.nature.com/doifinder/10.1038/nmat3115.

[31] Tobias A. Schaedler et al. "Ultralight metallic microlattices". In: *Science* 334.6058 (2011), pp. 962–965. ISSN: 0036-8075. DOI: 10.1126/science.1211649. URL: http://www.sciencemag.org/cgi/doi/10.1126/science.1211649.

[32] Siegfried Schmauder and Markus Meyer. "Correlation between dundurs ' parameters and elastic constants". In: *Z.Metallkd.* 83.1 (1992), pp. 524–528. ISSN: 00443093.

[33] John E. Strawley. "Wide range stress intensity factor expressions for ASTM E 399 standard fracture toughness specimens". In: *American Society for Testing and Materials*. Orlando Florida, 1976, pp. 1–4.

[34] Hiroshi Tada, Paul C. Paris, and George R. Irwin. *The Stress Analysis of Cracks Handbook*. Third. New York, NY: ASME Press, 2000. ISBN: 9780819492487.

[35] Harika C. Tankasala, Vikram S. Deshpande, and Norman A. Fleck. "2013 Koiter Medal Paper: Crack-tip fields and toughness of two-dimensional elastoplastic lattices". In: *Journal of Applied Mechanics* 82.9 (2015), p. 091004. ISSN: 0021-8936. DOI: 10.1115/1.4030666. URL: http://appliedmechanics.asmedigitalcollection.asme.org/article.aspx?doi=10.1115/1.4030666.

[36] Harika C. Tankasala, Vikram S. Deshpande, and Norman A. Fleck. "Tensile response of elastoplastic lattices at finite strain". In: *Journal of the Mechanics and Physics of Solids* 109 (2017), pp. 307–330. ISSN: 00225096. DOI: 10.1016/j.jmps.2017.02.002.

[37] Lorenzo Valdevit et al. "Compressive strength of hollow microlattices: Experimental characterization, modeling, and optimal design". In: *Journal of Materials Research* 28.17 (2013), pp. 2461–2473. ISSN: 0884-2914. DOI: 10.1557/jmr.2013.160. URL: http://www.journals.cambridge.org/abstract_S088429141300160X.

[38] Lorenzo Valdevit et al. "Protocols for the optimal design of multi-functional cellular structures: From hypersonics to micro-architected materials". In: *Journal of the American Ceramic Society* (2011), pp. 1–20. ISSN: 00027820. DOI: 10.1111/j.1551-2916.2011.04599.x.

[39] Xin-Tao Wang, Xiao-Wen Li, and Li Ma. "Interlocking assembled 3D auxetic cellular structures". In: *Materials & Design* 99 (2016), pp. 467–476. ISSN: 02641275. DOI: 10.1016/j.matdes.2016.03.088. URL: http://linkinghub.elsevier.com/retrieve/pii/S0264127516303719.

[40] R J H Wanhill. *Milestone Case Histories in Aircraft Structural integrity Milestone Case Histories in Aircraft Structural integrity*. Tech. rep. National Aerospace Laboratory, 2002, pp. 1–25.

[41] Xiaoyu Zheng et al. "Ultralight, ultrastiff mechanical metamaterials". In: *Science* 344.6190 (2014), pp. 1373–1377.

[42] Cheng Zhu et al. "Highly compressible 3D periodic graphene aerogel microlattices". In: *Nature Communications* 6 (2015), pp. 1–8. ISSN: 20411723. DOI: 10.1038/ncomms7962. URL: http://dx.doi.org/10.1038/ncomms7962.

[43] Elizabeth A. Zimmermann et al. "Biomaterials fracture resistance of human cortical bone across multiple length-scales at physiological strain rates". In: *Biomaterials* 35.21 (2014), pp. 5472–5481. ISSN: 0142-9612. DOI: 10.1016/j.biomaterials.2014.03.066. URL: http://dx.doi.org/10.1016/j.biomaterials.2014.03.066.

Appendix A

Cuboct Fracture: Geometry and Density Calculations

Most lattices are idealized in theory by pin-jointed beams. In practice, however, the beams must connect at a node, which leads to a finite node volume and deviation from ideal relative density as given by Equation (3.2). The exact geometry of the printed cuboct is described below, along with exact relative density calculations.

The lattice geometry used in this study is described by 3 parameters, the strut width w, pitch (unit cell length) p, and chamfer factor CF. The chamfer factor controls the relative size of the node, and is defined as

$$CF = \frac{w}{X}$$

where the node reinforcement height, X, is defined in Figure A.1.

Referencing Figure A.1, it can be shown that

$$h_1 = w \sin \pi/4 + w/2$$

$$h_2 = h_1 + X$$

$$h_3 = l_2$$

$$l_0 = X$$

$$l_2 = w/2 + X = \frac{h_2}{h_1}\frac{w}{2} = (1 + \frac{X}{h_1})\frac{w}{2}$$

$$l_3 = w \cos \pi/4$$

To calculate the volume of the node,V_n, subdivide the node into various sub-volumes shown in Figure A.2. To enable the calculation of the subvolumes, additional lengths are defined:

$$l_4 = l_2 + w \cos \pi/4$$

$$l_5 = \sqrt{2X^2} = \sqrt{2}X$$

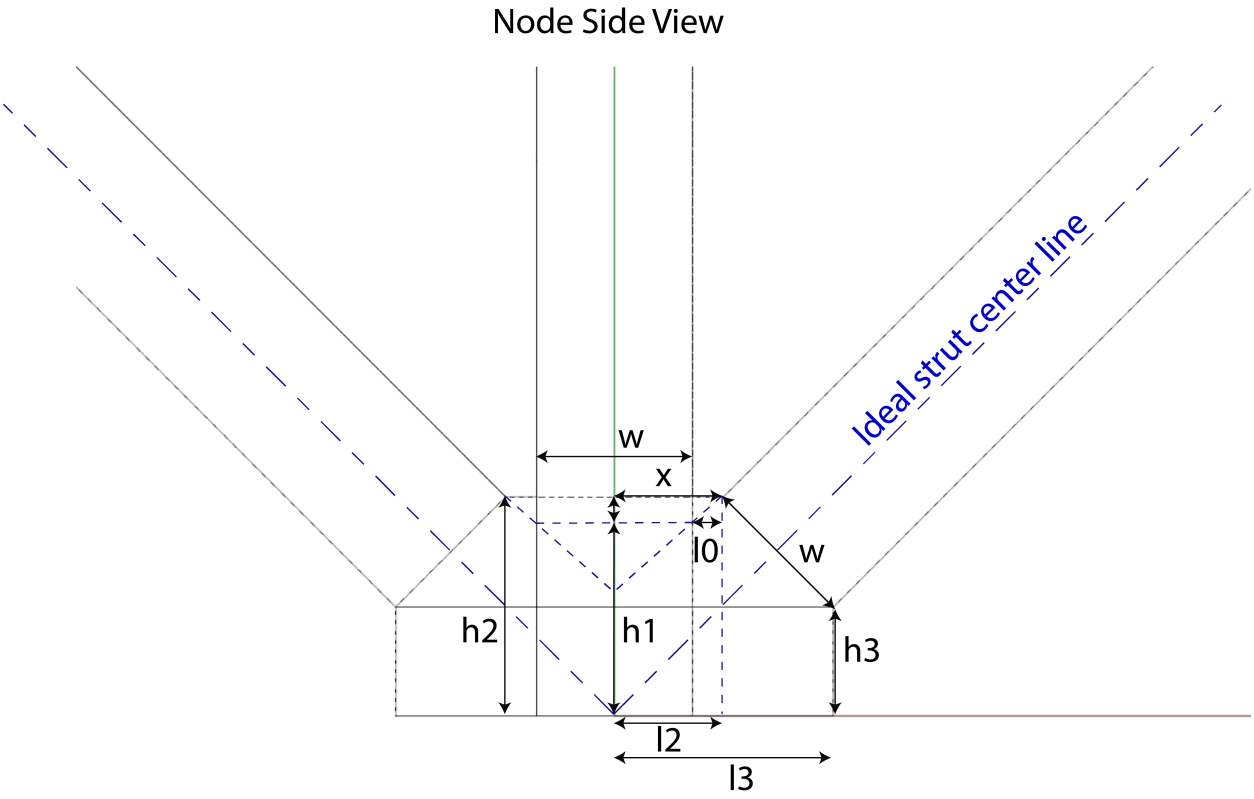

Figure A.1: Geometry of the printed cuboctahedral lattice node.

$$h = \tan\theta \frac{l_4}{2}$$

$$h_s = \tan\theta \frac{\sqrt{2}X}{2}$$

We can then calculate the subvolumes, the sum of which is the node volume V_n:

$$V_1 = h_3(w^2 + 4(w)(l_3 - w/2) + 4(1/2)(l_3 - w/2)^2$$

$$V_2 = \frac{l_4^2 h - 2X^2 h_s}{3}$$

$$V_3 = 4w(0.5(l_3 - l_2)(l_3 - l_2) + (l_3 - l_2)X)$$

$$V_4 = w^2(l_3 - l_2)$$

$$V_n = V_1 + v_2 + v_3 + v_4$$

The strut volume is the strut length, l_s times the cross-sectional area.

$$V_s = wwl_s$$

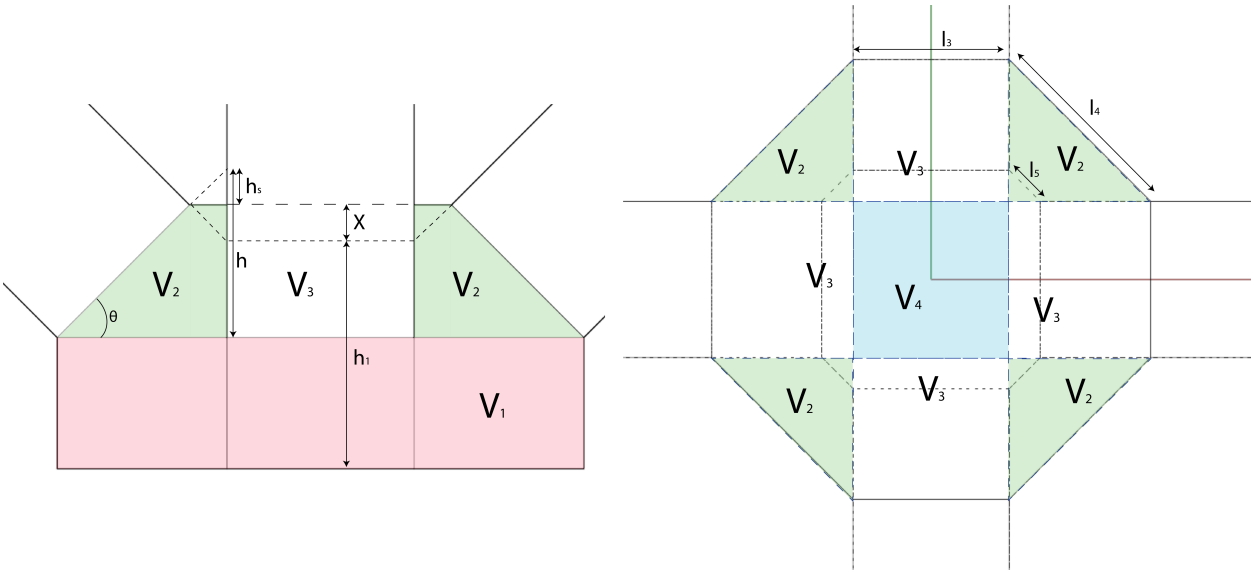

Figure A.2: Sub-volumes of the cuboctahedral lattice node used in volume calculations.

where l_s is given by

$$l_s = \frac{\sqrt{2}}{2}p - \sqrt{2}(l_2 + l_3)$$

Therefore the voxel volume, can be written as

$$V_v = 6V_n + 12V_s$$

and the relative density can be written as

$$\bar{\rho} = V_v/p^3$$

.

We can compare this exact relative density with the idealized relative density in Equation (3.2). Figure A.3 shows that the error in the idealized relative density increases at increased relative density. For this study, a chamfer factor, CF, of 5 was used, and accordingly, the maximum error in relative density if using the ideal calculation would have been 10 %. For this reason, the exact relative density was calculated using the above calculations for all experimental specimens. Due to the already idealized nature of FEA analysis, the ideal relative density was used for the ABAQUS simulations.

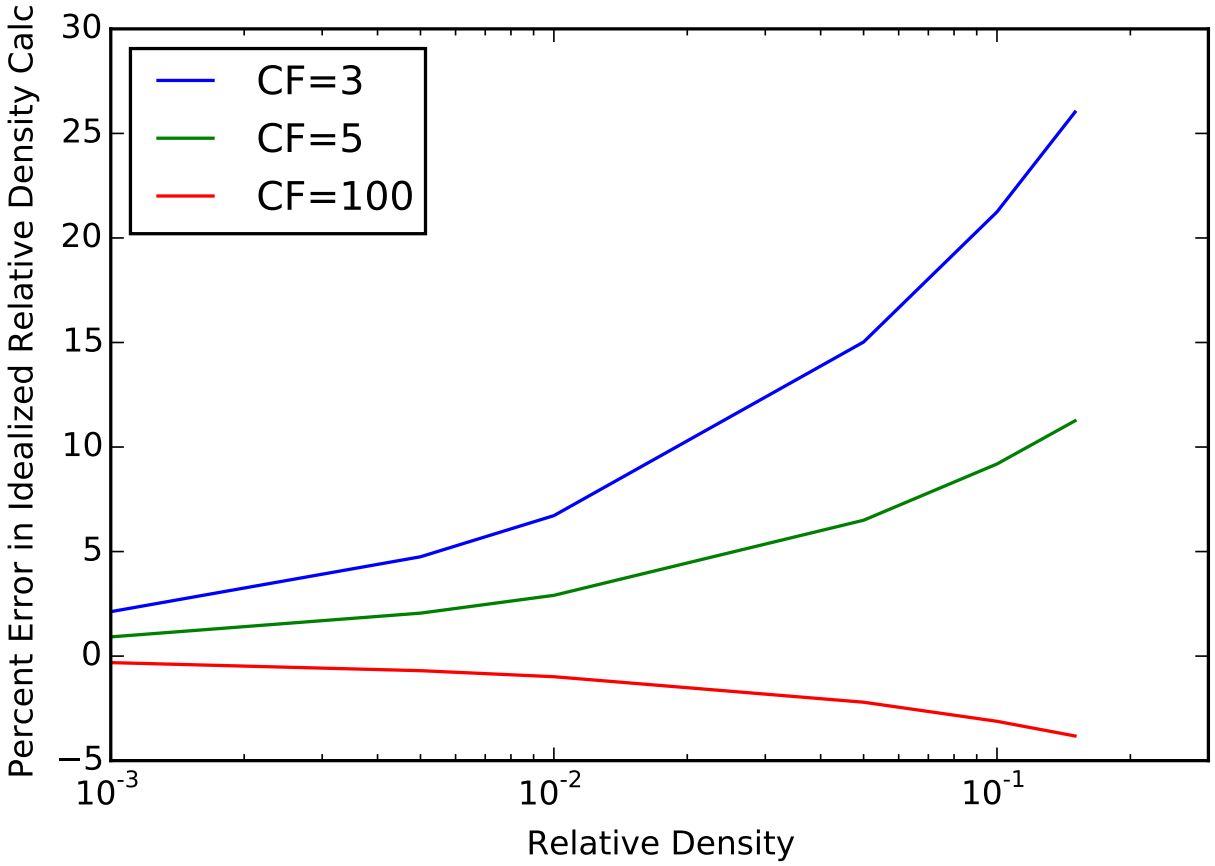

Figure A.3: Percent error of the idealized relative density when compared to the exact relative density of the printed model, for various chamfer factors. For all experiments, a chamfer factor of 5 was used. Notice that as relative density decreases, the affect of the node volume on the overall relative density decreases. Therefore, the percent error of the ideal relative density approximation decreases at lower relative density.